



Automated landslide detection outperforms manual mapping for several recent large earthquakes

David G. Milledge¹, Dino G. Bellugi², Jack Watt³, Alexander L. Densmore³

¹School of Engineering, Newcastle University, Newcastle upon Tyne, UK

5 ²Department of Geography, University of California, Berkeley, CA, USA

³Institute of Hazard, Risk, and Resilience and Department of Geography, Durham University, Durham, UK

Correspondence to: David G. Milledge (david.milledge@newcastle.ac.uk)

Abstract. Earthquakes in mountainous areas can trigger thousands of co-seismic landslides, causing significant damage, hampering relief efforts, and rapidly redistributing sediment across the landscape. Efforts to understand the controls on these landslides rely heavily on manually mapped landslide inventories, but these are costly and time-consuming to collect, and their reproducibility is not typically well constrained. Here we develop a new automated landslide detection algorithm (ALDI) based on pixel-wise NDVI differencing of Landsat time series within Google Earth Engine accounting for seasonality. We compare classified inventories to manually mapped inventories from five recent earthquakes: 2005 Kashmir, 2007 Aisen, 2008 Wenchuan, 2010 Haiti, and 2015 Gorkha. We test the ability of ALDI to recover landslide locations (using ROC curves) and landslide sizes (in terms of landslide area-frequency statistics). We find that ALDI more skilfully identifies landslides than published inventories in 10 of 14 cases when ALDI is locally optimised, and in 8 of 14 cases both when ALDI is globally optimised and in holdback testing. These results reflect both good performance of the automated approach but also surprisingly poor performance of manual mapping, which has implications not only for how future classifiers are tested but also for the interpretations that are based on these inventories. We conclude that ALDI already represents a viable alternative to manual mapping in terms of its ability to identify landslide-affected image pixels. Its fast run-time, cost-free image requirements and near-global coverage make it an attractive alternative with the potential to significantly improve the coverage and quantity of landslide inventories. Its simplicity (pixel-wise analysis only) and parsimony of inputs (optical imagery only) suggests that considerable further improvement should be possible.

25 1 Introduction

Landslides are important as agents of erosion and as a dangerous hazard (Marc et al., 2016; Froude and Petley, 2018). Large earthquakes or rainstorms can trigger thousands of landslides, redistributing tonnes of rock over distances of hundreds or thousands of metres within a few seconds (Li et al., 2014; Roback et al., 2018). These landslides can cause significant damage, hamper relief efforts, and rapidly redistribute sediment across the landscape. Efforts to understand the drivers, behaviour, and consequences of these landslides rely heavily on landslide inventories, in which landslide locations are mapped either as points, lines, or polygons, usually associated with one or more assumed trigger events. Landslide inventories are important because



they document the extent and impact of landslides in a region, informing disaster response and recovery (Williams et al., 2018); they capture the distribution, properties, and (through predictive models) drivers of landslides (Guzzetti et al., 2012, Tanyas et al., 2019); they train and evaluate models of landslide susceptibility, hazard, and risk (Van Westen et al., 2006; Reichenbach et al., 2018); and they enable geophysical flux calculations central to the study of landscape evolution and the global carbon cycle (e.g., Hilton et al., 2008; Marc et al., 2016). Landslide inventories were traditionally generated from expensive and time-consuming site visits (e.g., Warburton et al., 2008), severely limiting the number of landslides that could be mapped and thus the scale of enquiry. However, they are now increasingly collected remotely based on interpretation of satellite or aerial imagery, allowing the compilation of much larger datasets (e.g., Li et al., 2014; Roback et al., 2018).

40 Imagery provides an opportunity for rapid mapping over wide areas but is subject to some important limitations. For optical imagery, which depends on reflected solar energy reaching the sensor, cloud and shadow can obscure the ground surface. Active sensors, such as radar, that operate at wavelengths that are not reflected by cloud suffer from other issues (e.g., radar layover and shadowing) and their images are only recently being incorporated into operational landslide mapping approaches (e.g., Konishi and Suga, 2018; Burrows et al., 2019; Aimaiti et al., 2019; Mondini et al., 2019). Images may not be available

45 for the study area over the time window of interest, and - when they are available - they can be costly to acquire. In steep or high-relief topography, images can suffer severe geo-rectification errors (Williams et al., 2018), which is particularly problematic for landslide mapping because these are the areas of most interest. Imagery is becoming increasingly available across a very wide range of spatial and spectral resolutions but there remains a trade-off between resolution and cost, with 30 m imagery freely available globally with a 14-day revisit time (e.g., Sentinel 2, Landsat 8) while sub-metric resolution data

50 can be acquired on demand but at a cost of 10^1 - 10^4 USD/km² (e.g., Worldview, Pleiades). Landslides are typically identified in imagery either by automated classification, manual mapping, or some hybrid of the two. Manual mapping, although much faster than site visits, remains very time consuming over moderate to large areas (Galli et al., 2008), particularly for co-seismic inventories, which can involve digitising 10^4 to 10^5 landslides (e.g., Xu et al., 2014; Harp et al., 2016). It also requires comparison of pre- and post-event images to identify change and to avoid conflation of landslide

55 rates related to the trigger event with those before or after the event (e.g., Hovius et al., 2011; Marc et al., 2015). Automated classification can considerably speed up this process but is complicated by other factors, including: the range of possible landslide sizes and geometries; the non-unique signatures of landslides relative to roads, buildings, or other features; and the difficulty of excluding pre-existing landslides (Parker et al., 2011; Behling et al., 2014). Automated landslide classification has been demonstrated predominantly using high-resolution imagery and requires a high level of tuning, thus it is not

60 necessarily transferrable from one region or event to another. Imagery can be combined with other sources of information (e.g., slope inclination from DEMs) to remove some false positives, where a location is incorrectly classified as a landslide (Parker et al., 2011). This can improve classifier performance but can also generate spurious correlation when interpreting the results (e.g., landslide susceptibility with slope inclination). Some authors have adopted hybrid approaches; for example, Li et al. (2014) applied manual checking to the earlier automated mapping of Parker et al. (2011).



65 As a result of these issues, our database of landslide inventories is limited in number and biased towards the most spectacular
trigger events. This point is most easily illustrated by examining earthquake-triggered landslide inventories since in this case
the trigger event is generally very clearly identifiable in time and its footprint is well defined in space. Of the 326 earthquakes
known to have triggered landslides between 1976 and 2016, only 46 have published landslide maps (Tanyas et al., 2017). For
225 earthquakes the existence of co-seismic landslides was known from news reports and witness testimony (Marano et al.,
70 2010), but no reliable quantitative or spatial landslide data are available (Tanyas et al., 2017). Many other earthquakes have
likely triggered landslides, but these have gone unreported because they occurred out of human view. Between 1976 and 2016
there were ~6500 earthquakes sufficiently large ($>M_w$ 5), shallow (<25 km) and near to land (<25 km) to trigger landslides
(based on Marc et al., 2016). This suggests that the existing set of co-seismic landslide inventories is a small subset ($<15\%$) of
those earthquakes known to have triggered landslides and a tiny subset ($<1\%$) of those likely to have triggered landslides.

75 To extend the number of landslide inventories requires a reduction in the cost of inventory collection, both in terms of imagery
expense and mapping time. We hypothesise that recent improvements in satellite data management (e.g., data cubes) and
computing capabilities (e.g., cloud computing) have made it possible to collect automated landslide inventories of comparable
quality to manual mapping, and at a fraction of the cost, due to reductions in both imagery cost and mapping time. Imagery
cost could be reduced by using cheaper, lower resolution imagery, while mapping time could be reduced by using automated
80 detection rather than manual mapping. However, these savings will only represent value for money if they can deliver
inventories of comparable or superior quality to manual mapping.

Large amounts of freely-available optical imagery with near-global coverage have been generated by the Landsat and Sentinel
programmes. Landsat has been running for more than 30 years (since the Landsat 4 launch in 1982), imaging the majority of
the Earth's surface at a return time of c. 14 days and at 30 m spatial resolution through the visible and infra-red bands. Landsat
85 received early attention as a source of imagery for manual landslide mapping (e.g., Sauchyn and Trench, 1978; Greenbaum et
al., 1995) but has since been largely superseded by imagery with higher spatial resolution, which is often assumed to result in
more precise landslide mapping (e.g., Parker et al., 2011; Li et al., 2014; Roback et al., 2018). The recent HazMapper
application of Scheip and Wegmann (2021) is a notable exception, which seeks to leverage the large volume of freely available
coarser resolution imagery to provide information on vegetation change that can be used to map a range of hazards including
90 landslides. It is not clear, however, whether the long time series of coarser-resolution imagery that are now available contain
as much usable information as individual images of finer resolution.

There have been some attempts at automated landslide detection from Landsat (e.g., Barlow et al., 2003; Martin and Franklin,
2005). The results of automated detection algorithms have not typically been framed as a viable alternative to manual mapping,
however, but instead have been compared to a manual map of landslides that is assumed to be more accurate and considered
95 to represent the 'ground truth' (van Westen et al., 2006; Guzzetti et al., 2012; Pawłuszek et al., 2017). Automated or hybrid
approaches still need visual interpretation for calibration, sometimes over large areas (e.g., Đuric et al., 2017) and there remains
a perception in the landslide community that such techniques are neither necessarily more accurate (Guzzetti et al., 2012;
Pawłuszek et al., 2017) nor less time consuming (Santangelo et al., 2015; Fan et al., 2019) than manual interpretation. Given



100 the considerable investment of time and money involved in compiling an inventory, researchers continue to take a conservative approach and map by hand. It would therefore be useful to evaluate both automated classification and manual mapping against a common measure of performance.

Establishing the performance of an automated classifier against manual mapping requires both establishing the landslide characteristics that should be reproduced and establishing the quality of manual mapping with respect to these characteristics. Uncertainty in manually-mapped landslide inventories has received relatively little attention. However, the limited number of other studies that do quantify landslide inventory error all suggest very weak spatial agreement between different manually-mapped landslide inventories. Ardizzone et al. (2002) found 34-42% overlap between three inventories for the same study area (i.e., 34-42% of the area classified as a landslide in one inventory was classified as a landslide in another). Galli et al. (2008) found 19-34% overlap for three different inventories and Fan et al. (2019) found 33-44% overlap for three inventories associated with the Wenchuan earthquake. Fan et al. (2019) also compared their own inventory to the three published inventories and found overlaps of similar magnitude (32-47%) with two inventories but a much closer agreement (82% overlap) with the third; however, they do suggest a reason for this closer agreement. Importantly, inventories may differ not only in the locations of landslides but also in the geometry of the mapped landslides, particularly their area-frequency distributions (Galli et al., 2008; Fan et al., 2019; Tanyas et al., 2019).

This research seeks to: 1) test our hypothesis that an automated detection algorithm applied to time series of lower-resolution imagery can deliver inventories of comparable quality to those generated from manual mapping of higher-resolution imagery; and 2) address the problem that we don't currently have an objective comparison of manual mapping with automated classification. We address the first topic by introducing a new approach to automated landslide detection using Landsat time series in Google Earth Engine (GEE). Our approach uses similar data and architecture to HazMapper but is focused on landslides in particular and uses an expectation of long- and short-term change rather than a straight comparison of pre- and post-event composite images (Scheip and Wegmann, 2021). We address the second by applying this approach to case studies where there are at least two pre-existing inventories. This allows direct comparison of the inventories that we create (in terms of location and size) with multiple versions of 'ground truth'. The key question: can landslide location and size be reproduced more skilfully by our automated approach than by a second manual inventory?

2 Case study sites

125 We choose earthquake-triggered landslide detection to test our hypothesis because: 1) this type of trigger is well constrained in time and its footprint is well defined in space; and 2) there are several earthquake case studies for which at least two landslide inventories are available in order to assess the quality of manual mapping. We choose five earthquake case studies in which at least two landslide inventories have been published and where the authors attribute the landslides to the same trigger event (i.e., earthquake timing and epicentral location). The mapping times given below are each team's estimates of the total number



130 of person-days taken to map the landslides in their inventory; this is reported in the metadata associated with that team's
submissions to the USGS Science Base catalogue of landslide inventories (Science Base Community, 2021).
The 2005 Kashmir, Pakistan, earthquake triggered >2,900 landslides with a combined area of ~110 km² across an area of 4,000
km² (Basharat et al., 2016). The study area is primarily underlain by sedimentary rock with seasonal snow on the highest peaks
and has a summer monsoon climate (but is drier than the 2015 Gorkha study site). Landslides associated with the earthquake
135 were mapped by Sato et al. (2007; 2017), who estimated that they spent 60 days mapping the landslides using 2.5 m resolution
SPOT 5 optical satellite imagery, and by Basharat et al. (2016; 2017) over 90 days using 2.5 m resolution SPOT 5 imagery
and field reconnaissance. The inventories of Saito and Basharat contain 2,424 and 2,930 landslides respectively.
The 2007 Aisen Fjord, Chile, earthquake triggered >500 landslides with a combined area of ~17 km² across an area of 1,500
km² (Sepulveda et al., 2010). The study area is glacially carved valleys in volcanic rock and has a temperate climate with
140 seasonal snow throughout and perennial snow at altitude. The associated co-seismic landslides were mapped by Sepulveda et
al. (2010a; 2010b) over 120 days using Landsat images and field mapping, and by Gorum et al. (2014; 2017b) over 5 days
using 5 m resolution SPOT 5 imagery. The inventories of Sepulveda and Gorum contain 538 and 517 landslides respectively.
The 2008 Wenchuan, China, earthquake triggered >190,000 landslides with a combined area of ~1000 km² across an area of
75,000 km² (Xu et al., 2014). The study area is primarily underlain by meta-igneous and sedimentary rock with a humid
145 temperate climate and snow cover limited to the highest peaks. The associated co-seismic landslides were mapped by Li et al.
(2014; 2017) over 300 days using high (3-10 m) resolution optical satellite images, and by Xu et al. (2014; 2017) over 1200
days using high (1-20 m) resolution satellite images. The inventories of Li and Xu contain 69,606 and 197,481 landslides
respectively.
The 2010 Haiti earthquake triggered >20,000 landslides with a combined area of ~25 km² (Harp et al., 2016) across an area of
150 ~4,000 km². The study area is characterised by steep but low relief valleys cut through sedimentary rock with a humid
temperate climate in which snow is extremely rare and a land-use regime in which the vegetation is rapidly changing. The
associated co-seismic landslides were mapped by Gorum et al. (2013; 2017a) over 40 days using GeoEye-2 and Worldview-2
(0.6-1 m resolution) satellite images, and by Harp et al. (2016; 2017) using 0.6 m resolution aerial photographs and field
mapping. The inventories of Gorum and Harp contain 4,490 and 23,567 landslides respectively.
155 The 2015 Gorkha, Nepal, earthquake triggered >24,000 landslides with a combined area of ~87 km² across an area of 20,000
km² (Roback et al., 2018). The study area is primarily sedimentary and metamorphic rock with seasonal snow at higher
elevation and perennial snow and ice at highest elevations. The climate ranges from humid temperate to alpine with a strong
summer monsoon. The associated co-seismic landslides were mapped by Zhang et al. (2016, 2017) over 20 days using Gaofen
1 and 2 (1-5.8 m resolution) and Landsat satellite images; by Roback et al. (2017, 2018) using Worldview satellite images
160 (0.5-2 m resolution); and by Watt (2016). The inventories of Roback, Zhang and Watt contain 24,915, 2,643 and 4,924
landslides respectively. The Watt (2016) mapping reported here was undertaken for a period of 60 days and involved
comparing pan-sharpened false colour composites (red, green and near infra-red) derived from Landsat 8 images before and
after the earthquake. Mapping was undertaken from multiple images to minimise occlusion by cloud, but all images were



165 acquired within one year before and after the earthquake. The majority of the study area was mapped by a single person based on comparison of one pre- and two post-event images (from 13/3/2015, 1/6/2015, and 7/10/2015). This mapping was checked and supplemented by a second mapper using the same procedure to capture previously occluded areas using seven more Landsat 8 images.

3 Methods

3.1 ALDI classifier: theory

170 Landslides remove soil, vegetation, and sometimes bedrock, exposing bare regolith or rock in their scars and spreading a mantle of sediment over the ground surface downslope. In vegetated areas, landslides are most commonly identified in optical imagery by their removal (or occlusion) of vegetation with its distinctive ‘red edge’ spectral signature. Vegetation reduces reflected red energy due to vegetation pigment absorption and increases reflected near infra-red energy due to scattering by healthy leaves within the canopy (Colwell, 1974). This can be quantified using the normalised difference vegetation index
175 (NDVI; Tucker, 1979):

$$NDVI = \frac{R_n - R_r}{R_n + R_r} \quad (1)$$

where R_n is spectral reflectance in the near infra-red band and R_r is spectral reflectance in the red band (wavelengths in Table 1). The light reflected from landslide-affected pixels, whether they are within the scar or runout area, has a spectral signature associated with rock or sediment. This differs considerably from vegetation in terms of R_n and R_r , resulting in extremely low
180 NDVI values. Therefore, to capture the removal or occlusion of vegetation by landslides we utilise the NDVI change from before to after the trigger event, which we call dV , and which should be negative for landslide pixels associated with the trigger event. This is not in itself a novel approach and is similar to the other NDVI differencing approaches (e.g. Behling et al., 2014; 2016; Marc et al., 2019; Scheip and Wegmann, 2021).

In addition, vegetated areas disturbed by landslides regrow slowly (over timescales of years to tens of years). Thus, for
185 landslide affected pixels NDVI should not only reduce after the trigger event but also stay low for an extended period (at least one year). Therefore, we examine a time series of post-event images to calculate a time-averaged post-event NDVI, which we call V_{post} , and which should be low for landslide pixels associated with the trigger event.

Averaging over time series of images has the additional advantage that it enables robust estimates of both dV and V_{post} even for NDVI time series that are both patchy and noisy. The time series are patchy because cloud cover occludes the ground for
190 some pixels on some days; this cloud can be removed using filtering algorithms (e.g., Irish, 2000; Goodwin et al., 2013) but this leaves a gap in the time series. The timing and number of these gaps vary from pixel to pixel, making comparison of NDVI for particular dates or images problematic. The time series are noisy because atmospheric conditions alter both incoming radiation (e.g., cloud shadow) and that received by the sensor and because ground surface (and especially vegetation) properties



will vary over time both systematically (e.g., due to seasonal vegetation growth and harvesting) and randomly (e.g., due to leaf
 195 orientation).

Since the NDVI is both seasonally varying and noisy, dV and V_{post} should 1) normalise for seasonal change; and 2) record not
 only changes in average NDVI but also an indication of the probability that these changes are significant. This probability can
 be estimated by testing the probability that two NDVI samples were drawn from different distributions. Since seasonality can
 be a strong influence on NDVI a paired test accounting for the day of year on which the image was acquired is appropriate.
 200 Therefore, we also include the probability that NDVI values after the trigger are drawn from a significantly different
 distribution than those before the trigger, which we call P_t , and which should be high for landslide pixels associated with the
 trigger event.

Although low NDVI is effective for identifying the absence of vegetation, it does not uniquely identify landslides since a range
 of other surfaces generate similar signatures, particularly snow and cloud. Cloud cover varies from one image to another, and
 205 we thus seek to remove cloud-affected pixels from both the pre- and post-event time series. Cloud can be identified based on
 its spectral signature, with different types resulting in different signatures. The ‘Landsat simple cloudscore’ function within
 Google Earth Engine returns the minimum of a set of five cloudiness indices using equations 2a-f and parameters in Table 2
 (Earth Engine, 2021). Each index reflects an expectation about cloud reflectance and temperature: they should be reasonably
 bright in the blue band (CI_b), in all visible bands (CI_v), and in all infra-red bands (CI_{ir}); and they should be reasonably cool in
 210 temperature (CI_{Temp}); but they should not be snow (CI_{NDSI}):

$$CI_b = \frac{R_b - R_{bmin}}{R_{bmax} - R_{bmin}} \quad (2a)$$

$$CI_v = \frac{(R_r + R_g + R_b) - R_{vmin}}{R_{vmax} - R_{vmin}} \quad (2b)$$

$$CI_{ir} = \frac{(R_n + R_{s1} + R_{s2}) - R_{irmin}}{R_{irmax} - R_{irmin}} \quad (2c)$$

$$CI_{Temp} = 1 - \frac{Temp - Temp_{min}}{Temp_{max} - Temp_{min}} \quad (2d)$$

$$215 \quad CI_{NDSI} = 1 - \frac{NDSI - NDSI_{min}}{NDSI_{max} - NDSI_{min}} \quad (2e)$$

$$CI = \min(CI_b, CI_v, CI_{ir}, CI_{Temp}, CI_{NDSI}) \quad (2f)$$

Snow-covered pixels are generally more stable in time than cloud cover, thus we cannot retain sufficient observations to
 calculate stable statistics from these pixels. Instead we identify pixels where persistent snow cover could result in misleading
 statistics using the normalised difference snow index, NDSI:

$$220 \quad NDSI = \frac{R_g - R_s}{R_g + R_s} \quad (3)$$

where R_s is spectral reflectance in the shortwave infra-red band and R_g is spectral reflectance in the green band (wavelengths
 in Table 1).

We define the Automated Landslide Detection Index (ALDI) as the product of the three parameters defined above. While this
 formulation is arbitrary, it has the advantage of allowing the index to take a minimum value of zero (indicating negligible



225 probability of landsliding) if any of the individual terms is zero. Because we have no *a priori* knowledge of the relative importance of each parameter in determining landslide probability, we assume a power-functional form with empirical exponents α , β and λ :

$$ALDI = \begin{cases} (-dV)^\alpha (1 - V_{post})^\beta P_t^\lambda, & \text{if } S_{post} > T_{snow} \mid dV < 0 \\ 0, & \text{otherwise} \end{cases} \quad (4)$$

The likelihood that a pixel is landslide-affected increases monotonically with ALDI, which has upper and lower bounds of 0 and 1 respectively. Landslide pixels should be characterised by negative dV , indicating vegetation removal; low V_{post} , indicating a lack of vegetation after the earthquake; and high P_t , due to a large variance between pre-event and post-event NDVI distributions. The likelihood that a pixel contains a landslide should increase with P_t (range: [0,1]) and decrease with dV (range: [-1,1]) and V_{post} (range: [0,1]). Pixels with high NDSI could easily be misclassified as landslides but are instead more likely to be snow covered and thus should be classified as such. We thus exclude snow-dominated pixels where mean post-earthquake NDSI (S_{post}) exceeds a threshold (T_{snow}), as well as pixels where median post-earthquake NDVI exceeds that pre-earthquake (i.e., positive dV).

3.2 ALDI classifier implementation and data pre-processing

We implement ALDI and perform all pre-processing steps within Google Earth Engine (Gorelick et al., 2017) because: 1) it hosts an extensive Landsat archive and provides efficient access to large volumes of freely available satellite data; 2) it provides both a toolkit of pre-compiled algorithms for image processing and cloud computing resources to run these algorithms; and 3) it is an open access platform so that both the data and the algorithms used here are widely accessible and reproducible (source code available in Supplementary Information).

The objective of pre-processing is to generate four layers: dV , the change in NDVI before and after the trigger event; V_{post} , the time-averaged post-event NDVI; S_{post} , the post-event NDSI; and P_t , the probability that pre- and post-event NDVIs are drawn from different distributions. These layers should synthesise the time series of available imagery from multiple sensors minimising bias due to the sensor, the influence of clouds, and seasonal vegetation changes.

We use time series of NDVI calculated from Landsat 5, 7 and 8 imagery following ‘top of atmosphere’ correction (Chandler et al., 2009) to adjust for radiometric variations due to solar illumination geometry (angle and distance to Sun) and sensor specific gains and offsets. Sentinel 2 data would offer additional gains in terms of both spatial and temporal resolution of data but are not available for any of our case study events and thus cannot yet be evaluated within the same framework. Landsat 8 sensors aggregate red and near infra-red reflectance over slightly different frequency bands to Landsat 5 and 7 but their central frequencies vary by <4% between sensors and by >20% between bands (Table 1).

The time series is split into two ‘stacks’ of images, those before the trigger event and those after it (Figure 1b). The duration of these time series (and thus length of stacks) reflects a trade-off between shorter durations, which limit the sample size, and longer durations, which include landscape changes unrelated to the earthquake. We remove ‘cloudy’ pixels from each stack using the GEE simple cloud score exceeding a tuneable threshold (T_{cloud}) where stricter thresholds remove more cloudy pixels



but also incorrectly remove more cloud-free false positives (GEE, 2018). The number of images in each stack is controlled by the stack lengths and cloud threshold introducing three tuneable parameters to be calibrated.

260 To account for seasonal vegetation change, NDVI values for each pixel in the pre- and post-earthquake stacks are extracted as a time series (Figure 1a) and binned based on the month in which the image was acquired. Monthly bins are used since they are generally long enough to contain data in every bin (even after removal of cloudy pixels) but short enough to capture seasonal changes. We calculate median NDVI for each monthly bin, choosing median rather than mean since it is more robust to outliers (Figure 1c). We difference the monthly median values prior to and after the trigger event, generating a distribution of differences (Figure 1c). From that distribution, we calculate the mean monthly NDVI difference, dV , and the mean of the
265 post-event monthly NDVI, V_{post} . We then evaluate the likelihood that the mean monthly NDVI difference differs significantly from zero using a pairwise t-test to calculate P_t . A similar procedure is applied to the pixel-wise NDSI values to calculate the mean of the post-event monthly NDSI, S_{post} . This allows us to construct maps of the pixel-wise values of dV , V_{post} , S_{post} and P_t (Figure 1d) and thus to evaluate equation 4. The full routine runs in GEE in less than 30 minutes for an area of $\sim 10^4$ km² (c. 10^7 pixels).

270 3.3 Performance testing

We evaluated ALDI performance in terms of its ability to identify landslides from manually mapped inventories since these are widely accepted as the most accurate method to identify landslide locations. For each earthquake inventory we defined a study area based either on the study area defined by the manual mappers (e.g., excluding areas where cloud or snow cover hampered manual mapping); or on a convex hull that bounds the landslide inventory.

275 ALDI is a relative measure of the confidence with which a pixel is identified as a landslide. To evaluate this measure against a landslide map it must be converted into a binary classification by thresholding the classification surface. The benefit of a given classification can then be quantified in terms of success in classifying positive (landslide) and negative (non-landslide) outcomes on a pixel-by-pixel basis. Thresholding the classification surface is a difficult exercise involving a trade-off between sensitivity, the fraction of the landslides that should be captured (also known as the true positive rate, TPR - the number of
280 true positives normalised by all positive observations); and specificity, the number of false positives that should be allowed in doing so (also known as the false positive rate, FPR - the number of false positives normalised by all negative observations). In practice, this threshold is often set by external requirements in terms of a desired sensitivity or specificity, but these requirements can vary considerably between users and applications.

Receiver operating characteristic (ROC) curves provide a more complete quantification of the performance of the classifier
285 (e.g., Frattini et al., 2010). The ROC curve is constructed by incrementally thresholding the classifier and evaluating true and false positive rates at different threshold values to generate a curve where the 1:1 line reflects the naïve (i.e. random) case. The area under the curve (AUC) tends to 1 as the skill of the classifier improves towards perfect classification and to 0.5 as the classifier worsens towards the naïve (random) case. The strength of AUC is that it avoids the need to threshold the classifier



and is widely used, enabling comparison with other landslide detection methods; its main weakness is that it is difficult to
290 interpret in absolute terms. What AUC constitutes ‘good’ performance?

In our case, we seek to establish whether automated detection performance is such that it can be used as an alternative to
manual mapping. However, it is difficult to compare ALDI against manual mapping because manual mapping is itself being
used as the ‘ground truth’ in the absence of a better alternative. To address this, we first test the agreement between manual
inventories in terms of true and false positive rates. TPR_{I1-2} indicates the fraction of landslides in inventory I1 that are also
295 predicted by I2 and FPR_{I1-2} indicates the fraction of non-landslide pixels in I1 that are ‘incorrectly’ identified as landslide
pixels by I2.

ALDI performance can then be compared against one of the manual maps as a competitor with the other manual map used as
the check dataset. To enable the comparison, ALDI must first be thresholded to generate a binary classifier with the same FPR
as the competitor inventory with respect to the check inventory. The ability of ALDI to successfully identify more landslide
300 pixels than the competitor inventory can be calculated from the difference in their true positive rates, TPR_{diff} :

$$TPR_{diff} = TPR_{ALDI} - TPR_{Comp}, \quad FPR_{ALDI} = FPR_{Comp} \quad (5)$$

where: TPR_{ALDI} and FPR_{ALDI} are the ALDI true and false positive rates respectively, both calculated from the check inventory;
and TPR_{Comp} and FPR_{Comp} are the true and false positive rates for the competitor inventory, all calculated with respect to the
check inventory. The magnitude of TPR_{diff} indicates the similarity in performance while the sign indicates the best performer
305 (positive values indicate that ALDI out-performs manual mapping and vice versa). The strength of this approach is that it
allows direct comparison between automated and manual mapping; its weakness is that it imposes a single arbitrary threshold
on the classifier based on the FPR of the competitor dataset. In addition, we express spatial mapping error between manual
inventories as the ratio of the intersection of the two maps to their union. This is equivalent to the ‘degree of matching’ (Carrara
et al., 1992; Galli et al., 2008) and can be interpreted as the percentage of total mapped landslide area that the inventories have
310 in common.

3.4 Parameter calibration and uncertainty estimation

The ALDI landslide classifier has seven tuneable parameters: cloud threshold (T_{cloud}), pre-event stack length (L_{pre}), post-event
stack length (L_{post}), snow threshold (T_{snow}), and the three exponents (α , β and λ) that control the weighting assigned to the V_{post} ,
 dV and P_i layers respectively. Calibrating the parameters and estimating the associated uncertainty is important because the
315 parameters are difficult or impossible to set *a-priori* and because we seek to develop a general model that can be applied to
new landslide events not examined here. Our calibration seeks to optimize classifier performance evaluated by comparing the
classifier to 11 manually mapped landslide inventories using the performance metrics described in Section 3.3.

We calibrate ALDI parameters using one-at-a-time calibration for parameters that are internal to the GEE routine (T_{cloud} , L_{pre} ,
 L_{post}), since these parameters are well constrained (in the case of T_{cloud} and L_{post}) or have a limited number of possible values
320 (in the case of L_{pre} and L_{post}). We use an informal Bayesian calibration procedure (e.g., Beven and Binley 1992) for parameters
used in equation 4 (T_{snow} , α , β and λ) since these parameters are less well constrained but evaluation of equation 4 is



computationally cheap. We calibrate L_{pre} , L_{post} , and T_{cloud} , one-at-a-time, working from the most to least sensitive parameter for each earthquake event and then checking for interaction between parameters. For each GEE run in the one-at-a-time process we run 500 simulations of equation 4 with its parameters (T_{snow} , α , β and λ) randomly sampled from a uniform probability distribution across a parameter range wide enough to capture the optimum performance.

We examine L_{post} of up to five years because vegetation typically begins to re-grow over this timescale, and L_{pre} of up to ten years because we expect that other landscape changes will begin to disrupt the pre-event signal at longer timescales. In both cases we examine only integer year values to ensure consistent sampling within the monthly bins. We use the full range of NDSI values for T_{snow} ([0,1]) and cloudscore values for T_{cloud} ([0,1]). For the three exponents, we use zero for the lower bound and iteratively refined the upper bound to ensure that optimum performance at any site is found to be within the range.

We perform the calibration for individual earthquakes to estimate the optimum classification skill that could be obtained when calibrating on all the check data. We then combine the best 20 parameter sets (measured in terms of AUC) from each earthquake into a global parameter set. To account for parameter interaction within a set we retain parameter sets as 7-element vectors. To ensure that each manually mapped landslide inventory is given equal weight as a check dataset we calibrate to each in turn taking 7 parameter sets from calibration to each of the three Gorkha inventories, and 10 from each of the two inventories at the other sites.

Finally, we perform a holdback test in which we test ALDI for each site using the global parameter set but holding back the 20 parameter sets that were derived from the site at which testing is being performed. In this test the parameters used to generate ALDI are un-influenced by the specific behaviour of the test site – a proxy for ‘blind’ application of the classifier to future events.

3.5 Landslide size

Landslide hazard and landslide mechanics are both influenced by landslide size. Thus, a good landslide map would capture not only the locations of landslides (which can be captured by pixel-based presence/absence as in Section 3.3) but also their sizes. For manual mapping this information is generally captured automatically since landslides are mapped as discrete objects rather than on a pixel by pixel basis. However, automated classifiers like ALDI require additional steps to convert a continuous pixel-based classification surface to a set of landslide objects. First, we generate a binary prediction of landslide presence or absence by thresholding the continuous ALDI. Threshold choice is non-trivial and encodes an implicit weighting of the importance of TPR and FPR. We seek to match the weightings that characterise current practice in landslide mapping by thresholding ALDI at a value that generates a FPR equal to that generated by manual mapping, though we note that manual mapping tends to be characterized by conservatively low FPR (e.g. Table 3). Second, we convert the binary landslide map to a set of landslide objects by identifying connected components at the 30 m resolution of the Landsat imagery (Haralick and Shapiro, 1992). Finally, we calculate the area of individual landslide objects from the number of pixels in each object (cluster). This connected components clustering is one of the simplest of many possible clustering algorithms. Thus, we examine whether any misfit in size distributions is due to the patterns of identified landslides or to the clustering algorithm skill by converting



355 manual landslide maps to binary grids at 30 m resolution, performing the same connected component clustering, and
calculating the area of each cluster. The resultant size distributions are compared against one another and against those
generated directly from the mapped landslide polygons.

4 Results

4.1 Spatial agreement: Gorkha case study

360 We first illustrate our approach using the 2015 Gorkha earthquake, where three manual inventories are available, and then
consider the other five earthquakes introduced in Section 2. All three manual inventories for the Gorkha earthquake show an
elongated cluster of landslides extending from northwest to southeast (Figure 2a) that coincides with the area of steep slopes
that experienced the most intense shaking. However, when the maps are compared at a finer scale they differ considerably
(Figure 2c,e). In some cases, one mapper has identified a landslide but one or both of the others have not (e.g., location A in
365 Figure 2e). Some, but not all, of these missed landslides can be attributed to areas where imagery was unavailable or where
the ground was obscured by cloud (shown as grey or green areas in Figure 2c). In other cases, mapped landslides overlap but
their size and/or shape differ, due either to differences in interpretation of landslide boundaries (e.g., location B in Figure 2e)
or to the georeferencing of the underlying imagery from which the landslides were mapped. Georeferencing differences seem
particularly likely to explain mapped landslides of very similar size and shape that are offset by small distances (e.g., location
370 C in Figure 2e), or appear warped relative to one another so that their outlines only partially overlap (e.g., location D in Figure
2e).

The ALDI classifier applied to the Gorkha earthquake captures the broad spatial pattern of mapped co-seismic landslides with
large patches of high ALDI values, and thus high classification confidence, corresponding to clusters of mapped landslides
(Figure 2b). However, there are also a number of false positives in the south and west of the study area. A detailed look at a
375 subsection of the study area suggests that most of the landslides that are included in both inventories overlap areas of high
ALDI values (Figure 2d-e). In addition, areas of high ALDI values overlap many of those landslides identified by one inventory
but not the other (Figure 2e). In many cases the shape of the high-ALDI zone closely follows that of the mapped landslide
(Figure 2e). In other cases, patches of high ALDI values have typical landslide morphology but are not in either inventory
(e.g., location E in Figure 2e), raising the question of whether these should be considered genuine classifier false positives or
380 are in fact landslides missed in all three manual maps. Given that each inventory misses landslides identified by another, this
possibility cannot be excluded. In other cases, the patches of high ALDI values have a size and/or shape that suggests that they
are misclassifications. These may be due to cloud, shadow, snow or other landscape changes not associated with landslides
(e.g., crop harvesting, river channel change, building construction).



4.2 ALDI calibration: Gorkha case study

385 In this section, we seek to establish the best possible ALDI performance when parameters can be optimised to a single study
site and identify the influence of parameters on that performance, both in terms of sensitivity to the parameter and preferred
range for the parameter. We illustrate this using the Gorkha earthquake, calibrating ALDI's seven tuneable parameters
(columns A-G in Figure 3) to optimise agreement with two of the manually mapped landslide inventories measured using our
two performance metrics (rows in Figure 3). The results are visualised in Figure 3 using dot plots (after Beven and Binley,
390 1992): a matrix of scatter plots where each subplot shows model performance (y-axis) against a parameter value (x-axis). The
histogram above each scatter plot shows the frequency distribution of parameter values for the best 50 model runs for that
metric and check dataset.

All the scatter plots in Figure 3 show wide scatter in performance for a single value of any given parameter, indicating that the
model is sensitive to multiple parameters. However, the key feature of each plot is the upper bound on ALDI performance for
395 a given parameter value, and its sensitivity change in that parameter. This upper bound can be interpreted as the best possible
ALDI performance at value x of parameter A when all other parameters are given flexibility to optimise. Plots where this upper
bound is near horizontal suggest limited influence of a particular parameter and are accompanied by broad histograms. Narrow
peaks in a plot's upper bound indicate that good model performance requires that parameter to be set within a narrow range
with performance degrading rapidly as values depart from this range independent of other parameter values. In the following
400 paragraphs we examine the influence of each parameter in turn (Figure 3).

Setting the pre- and post-earthquake stack lengths (L_{pre} and L_{post} respectively) involves a trade-off between: errors caused by
landslides (or other landscape changes) not associated with the earthquake, if the stack is too long; and errors caused by cloud
cover, if the stack is too short. For the Gorkha earthquake, ALDI performance is most sensitive to L_{posts} , indicated by the steep
gradient in upper bound performance across all metrics and for all check datasets (Figure 3, column G). For all metrics and
405 datasets, a post-earthquake stack length of only one year produces the best performance. This may be because longer stacks
are more likely to include other landscape changes after the earthquake that disrupt the signal, such as post-seismic landslides
or re-vegetation of co-seismic landslides.

ALDI includes a snow mask that only allows landslides to be identified in pixels where NDSI is lower than the snow threshold
(T_{snow}). ALDI performs well (i.e. <20% from optimum) for T_{snow} values ranging from 0.1 to 0.9 (Figure 4, column D). For
410 TPR_{diff} the best values of T_{snow} are 0.2-0.4 with a rapid decline in performance as T_{snow} is reduced and a slow decline as it is
increased (Figure 4, panels D1-2 and D3-4). This suggests that snow rarely causes false positives even when little effort is
made to remove it, but that an overly conservative snow threshold results in landslides being misclassified as snow. The AUC
metric behaves similarly to the other two metrics with a larger performance reduction at low T_{snow} values and reduced
performance reduction at high T_{snow} values (Figure 4, D5-6). This reflects the increased cost of an overly-conservative mask at
415 less conservative ALDI thresholds. The snow mask is useful in removing false positives but unhelpful when it masks landslide
pixels that have been incorrectly identified as snow.



The $\alpha:\beta$ ratio controls the influence of change in NDVI (dV) relative to mean post-earthquake NDVI (V_{post}). ALDI is thus dominated by dV at higher ratios, and by V_{post} at lower ratios. There is a clear optimum within the parameter space and a large reduction in performance away from this optimum indicating that both layers (dV and V_{post}) are important components of the classifier (Figure 3, column B). Best performances are found in the range $\alpha:\beta = 3-4$ for TPR_{diff} and in the range $\alpha:\beta = 10-20$ for AUC, suggesting that more weight needs to be given to dV to successfully identify landslides, particularly when bulk performance over the full ROC curve is of primary concern.

The $\alpha:\lambda$ ratio controls the influence of change in NDVI (dV) relative to the (t-test derived) probability that the values in the post event stack are significantly different from the pre event stack (P_t). ALDI performance is sensitive to this parameter for TPR_{diff} , but not AUC, which varies by <3% across the full parameter range (Figure 3, column C). P_t clearly adds more value than dV for the Gorkha case study: performance worsens by ~79% for TPR_{diff} when dV rather than P_t is used. However, best performances are found within the parameter space and exclusion of either layer results in performance losses of >14% for P_t or >4% for dV indicating that both layers add value and should be retained. Optimum performance always involves $\alpha:\lambda < 1$, suggesting that: 1) NDVI difference should be given less weight than the more complete t-test derived probability; and 2) the additional information on pixel variability provided in the t-test does adds considerable value to ALDI for this site.

Optimum parameters for the Gorkha study site differ slightly between performance metrics (compare histograms down columns in Figure 3). This reflects the different focus of the metrics, where TPR_{diff} gives the strongest weight to very conservative (i.e. low FPR) classification thresholds (Figure 3, rows 1-2), and AUC weights all classification thresholds equally (Figure 3, rows 5-6). In general, the parameters to which ALDI performance is most sensitive are also those for which optimum values are most robust to changes in check dataset or performance metric. There is negligible change in optimum values for L_{post} and T_{snow} across the range of metrics and datasets. $\alpha:\beta$ and $\alpha:\lambda$ are both broadly comparable between metrics although in both cases there is a shift towards higher optimum values for AUC, indicating that for this metric NDVI difference increases in importance (noting that the improvement is always <3%). $\alpha:\beta$ has a progressively less clear optimum as metrics become more generalised (from TPR_{diff} to AUC) indicating reduced parameter sensitivity for AUC. T_{cloud} and L_{pre} have larger changes in optimised parameters, though the sensitivity to these changes is small in performance terms (Figure 3 columns 5-6). Optimum T_{cloud} is 0.7 for TPR_{diff} but 0.5 for AUC, optimum L_{pre} is in the range 2-5 for TPR_{diff} and 5-10 for AUC. ALDI performance is insensitive to α , varying by <10% across the parameter range for all metrics, generating a broad histogram of best-performing parameter values and showing large shifts in optimum value depending on both the metric and the dataset used to assess performance (Figure 3, column A).

4.3 ALDI calibration: global comparison

We focus our global comparison on the AUC performance metric. Other metrics produce very similar results and can be found in the supplementary information (Figures S1-S6). Figure 4 shows: that optimum values for a given parameter differ between



sites; that sensitive parameters at one site are usually sensitive at others; and that absolute performance differences between inventories at a site can be large but the trends are generally similar for different inventories at the same site.

450 ALDI is sensitive to L_{post} for all sites but with trends that differ between sites: for Haiti and Gorkha one year is best, two years is reasonable and three years is poor; for Kashmir and Wenchuan one year is best but two also gives reasonable results; for Aisen five years is best and one year is particularly poor (Figure 4 column G). An L_{post} of two years generally results in fairly good performances for all five sites. ALDI is sensitive to T_{snow} in 3/5 sites and particularly sensitive for Aisen, but in all cases T_{snow} of 0.5-0.8 results in performances that are close to, if not, optimum (Figure 4, column D). ALDI is only weakly sensitive
455 to L_{pre} for all sites and with subtly differing trends: for Kashmir three years is best, for Wenchuan and Haiti 10 years is best and for Aisen and Gorkha best performances are in the range of five to 10 years (Figure 4, column F). However, the trends are not linear and an L_{pre} of five years generally results in fairly good performances for all five sites. ALDI is generally insensitive to T_{cloud} across the range 0.3-0.7 with best performances consistently found at 0.5 though these are at most 10% better than those for other values in the range (Figure 4, column E). ALDI is insensitive to α alone, but is strongly sensitive to $\alpha:\beta$ and
460 weakly sensitive to $\alpha:\lambda$ at all sites (Figure 4, columns A-C) with best performances found for $\alpha:\beta$ in the range 1-100. ALDI application would be both faster and simpler if single optimum values could be used for the three parameters that define compilation and treatment of image stacks within Google Earth Engine (T_{cloud} , L_{pre} , L_{post}). Our site by site calibration suggests that it is possible to find single values for these parameters that result in good performance for all study sites (Figure 4). This is the case when the cloud threshold T_{cloud} is 0.5, the pre-earthquake stack length L_{pre} is 5 years, and the post-earthquake stack
465 length L_{post} is 2 years. We also examined performance when these parameters were allowed to vary but found that the performance improvement for the global parameter set was negligible.

To examine similarity between locally optimised parameters and compare them to a global set of parameter sets we first identified the best 96 parameter sets for each study site, using AUC as the performance metric (Figure 5). To generate the global parameter sets we held T_{cloud} , L_{pre} and L_{post} constant at 0.5, 5 years and 2 years respectively; then, treating the remaining
470 parameter sets as 4-element vectors, we sampled the best 20 parameters from each site; finally, we generated a holdback parameter set for each site by removing that site's parameters from the global set. Locally optimised parameter sets (grey histograms in Figure 5) are broadly consistent with the global set (blue histograms) with a small number of exceptions: T_{snow} should be set lower for Kashmir and higher for Aisen, $\alpha:\beta$ should be set higher for Kashmir and $\alpha:\lambda$ set lower for Gorkha. These differences are accentuated in the holdback distributions (the black outlined histograms) because the divergent local
475 parameter values are stripped from the set pulling the distributions away from their local optima. We would expect larger performance degradation from local to global to holdback parameter sets at sites where these distributions are more different. ALDI with locally optimised parameters always out-performs the global parameters and the global parameters always out-perform the holdback parameters (Table 3). The difference between local and global parameters is generally larger than between global and holdback parameters. In fact, performance reduction from global to holdback parameters is always <1%
480 for AUC. This indicates that the five study sites provide an adequately varied calibration set to enable generation of a general parameter set that is not overly influenced by any one site. This is encouraging for future 'blind' ALDI application. However,



the difference in performance between local and global parameters shows that local optimisation can improve ALDI performance in terms of AUC by up to 9% (and by 2% on average). In three cases, one for Kashmir and two for Gorkha, local optimisation improves ALDI to the point where it is no longer out-performed by the manually mapped competitor inventory but instead out-performs it. This is somewhat consistent with the observed divergence of locally optimised parameter distributions from the global distribution at these sites (Figure 5). However, it likely also reflects the broadly similar performance (i.e. skill) of ALDI and manual mapping at the sites (Table 3).

4.4 Spatial agreement: global comparison to manual mapping

Spatial agreement between manual landslide inventories is surprisingly low not only for the Gorkha study site shown in Figure 2 but across all sites. TPRs range from 0.08-0.8 indicating that at best 80% and at worst 8% of the landslide area mapped by one inventory is also identified as a landslide by a second test inventory (Figure 6a and Table 3). FPRs range from 0.0003-0.03, indicating that at best 0.03% and at worst 3% of the area that is identified as non-landslide in one inventory is instead identified as a landslide by a second test inventory. FPRs are more than an order of magnitude lower than TPRs for two reasons: 1) landslide density is low, so there are few positives (TP+FN) and many negatives (TN+FP); these are the denominators of TPR and FPR, respectively, amplifying TPR and damping FPR; and 2) landslide mappers tend to be conservative, mapping only features that they are confident are landslides. TPRs and FPRs are positively correlated but with considerable scatter (Figure 6a). In some cases manual maps agree quite closely: for example, the inventories of Gorum et al. (2013) and Harp et al. (2016) for Haiti (H_{GH} and H_{HG}) or those of Zhang et al. (2016) and Watt for Gorkha (G_{ZW} , G_{WZ}). These cases have a relatively high TPR given their FPR and plot towards the top left of the point cloud in ROC space (Figure 6a). In other cases the agreement is weaker, such as between the inventories of Li et al. (2014) and Xu et al. (2014) for Wenchuan (W_{LX} , W_{XL}) or those of Saito et al. (2007) and Basharat et al. (2016) for Kashmir (K_{SB} , K_{BS}). There is a symmetry to the inventory comparison because each inventory takes a turn as the competitor dataset (to which ALDI is being compared) and as the check dataset (against which both are evaluated). As a result, a single pairwise comparison results in two points in Figure 6a reflecting the switching of roles. The three-way comparison for the Gorkha earthquake results in three pairwise comparisons and six points. When one inventory is considerably more complete and less conservative then the separation between pairs of points will be large (e.g. Watt and Zhang for Gorkha). Zhang et al. (2017) reported, in their metadata, that their inventory is incomplete and focusses on the largest landslides, while that of Watt was more complete and less conservative. As a result Zhang et al. (2016) successfully identified only 10% of the landslide pixels identified by Watt but identified only a tiny fraction (<0.1%) of the study area as landslides when Watt considered that they were not (G_{ZW} in Figure 6a). Conversely, Watt's inventory successfully identified 80% of the landslides identified by Zhang et al. (2016), but also identifies a further 1% of the study area as landslides that were not identified as such by Zhang et al. (2016) (G_{WZ} in Figure 6a).

To evaluate ALDI performance relative to manual mapping, we compare the ability of ALDI to successfully identify more landslide pixels in one (check) inventory than another (competitor) inventory when ALDI is thresholded to reproduce the FPR of the competitor inventory. This TPR difference (TPR_{diff}) is shown as a red line in Figure 6b-f; positive differences indicate



515 that ALDI outperforms manual mapping and vice versa. ALDI outperforms manual mapping in the majority of cases when
parameters are locally optimised (10 of 14 cases, Figure 6 and Table 3) and is comparable to manual mapping when a single
global parameter set is applied to all study sites (8 of 14 cases). Performance is only slightly reduced when the test site is held
back from the global optimisation and ALDI continues to outperform manual mapping in 8 of 14 cases.

ALDI performs better at some sites than others, with performances at Aisen and Gorkha particularly good (Table 3).
520 Performance is poor for Haiti, both in absolute terms and relative to the manual mapping. For AUC, an indicator of absolute
performance, ALDI performance for the Haiti case is ranked 10th-11th of 14 (where the range results from combining local
global or holdback tests). Relative to manual mapping, ALDI correctly identifies 51-74% fewer landslide pixels for the same
FPR. Explanations for these performance differences are discussed in Section 5.4. ALDI in Wenchuan performs only
moderately in absolute terms, with ranked performances in the range 9th to 12th out of 14 for AUC, but out-performs manual
525 mapping (1st and 4th for TPR_{diff}) as a result of the relatively poor agreement between manual maps for the site. Kashmir has
very marked differences in ALDI performance depending on the test dataset (all <4th of 14 for Sato et al. (2007); all >9th of 14
for Basharat et al. (2016)), illustrating the difficulty of interpreting performance relative to check data when the check data
themselves contain errors of similar magnitude to the data being tested.

4.5 Size distributions

530 Probability density functions for landslide size in terms of the area of manually-mapped landslide polygons (Figure 7a-e)
follow a consistent distribution with a roll-over and a heavy right tail that is approximately linear in logarithmic space but that
usually has positive (convex up) curvature or a roll-off at very large areas. These characteristics have already been widely
reported both for the study inventories in particular (e.g., Gorum et al., 2013; Li et al., 2014; Roback et al., 2018) and for many
other landslide inventories worldwide (e.g., Tanyas et al., 2019). Different inventories for the same study site show broadly
535 consistent scaling in their right tail but tend to differ markedly in the location of the roll-over, modal size, degree of curvature
in their right tail and the location (and presence) of a roll-off for very large areas (e.g., Figure 7a, d and e). These differences,
and their possible explanations, have also been widely reported for these and other sites (see review by Tanyas et al., 2019).
The size distributions derived from ALDI and those from resampled manual mapping generally exhibit a broadly similar right
tail to those of the manually mapped distributions. Both sets of distributions have a heavy right tail that closely approximates
540 a power law, and both have similar scaling (i.e. slope in logarithmic space) in that right tail. However, these grid-based
distributions, which reflect the sizes of clustered landslide-affected areas (rather than the size of landslide objects themselves)
are clearly different from those derived from manual mapping. They lack the roll-over at small areas, the positive curvature,
and the roll-off at very large areas. These differences can be explained in terms of amalgamation and censoring. Amalgamation
of multiple neighbouring landslides increases the frequency of large landslides, fattening the right tail. Re-sampling to a 30 m
545 grid makes it impossible to record landslides smaller than a single pixel (i.e. 900 m²), censoring them from the size distribution.
The application of a ‘majority area’ rule in identifying a pixel as ‘landslide affected’ enhances the frequency of landslides that
are small but above the censoring threshold. For example, a landslide with an area of 500 m² contained within a single pixel



would result in a resampled area of 900 m²; a landslide with an area of 1000 m² split evenly between two pixels would result in a resampled area of 1800 m².

550 There is good agreement between cluster size distributions for landslide pixels classified with ALDI and those identified by resampling manual maps. This is the fairest evaluation of the classifier in its current form since no attempt has been made to identify or disambiguate landslide objects. However, the similarity in both mapped and classified cluster size distributions between sites suggests that this may be a somewhat blunt tool in evaluating classifier performance.

5 Discussion

555 5.1 The problem of testing against check data of only comparable quality

In the TPR_{diff} cross-comparison the ALDI classifier out-performs 8 of 14 inventories when tested against a second inventory indicating that it is more skilful than at least one of the inventories (either the check or competitor inventory). However, we are unable to a) conclude whether it is better than one or both inventories nor b) identify which inventory is better. This is because errors in a single inventory influence the result both when it is used as the predictor (i.e. as a competitor against ALDI) and the check dataset (against which both are evaluated). For four of the nine inventory pairs (Aisen; Wenchuan; Roback-Watt, Gorkha; and Roback-Zhang, Gorkha) the globally calibrated ALDI is more similar to each inventory than the inventories are to one another. This indicates either: a) that both inventories contain some errors and the ALDI contains fewer than either of them; or b) that ALDI contains similar errors to at least one inventory. In the latter case, pixels misclassified as landslides in one inventory (but correctly identified in the other) would also be misclassified as landslides by ALDI.

565 5.2 Performance differences in manual mapping reflect inventory errors, not solely mapping errors

Our findings on the large locational mismatch between co-seismic landslide inventories are initially surprising, given the widespread assumption that such inventories represent a 'ground truth' and the limited attempts to propagate these errors into hazard maps, classification tests, process inferences, or landslide rate estimates. However, the limited number of other studies that do quantify landslide inventory error all suggest very weak spatial agreement between landslide inventories (Ardizzone et al., 2002; Galli et al., 2008; Fan et al., 2019).

570 The process of generating a landslide inventory from satellite imagery involves choosing which images to map from and how to post-process and georeference them before landslides can be identified and delineated by a human mapper. Thus, the comparison of two inventories is not a direct test of the consistency with which human mappers detect and delineate landslides but instead the consistency with which different research groups generate landslide inventory maps. Fan et al. (2019) tested uncertainty due to differential mapping choice and ability. They found that landslide inventories had an overlap of 67%-86% (and 76% on average) when comparing between mappers in the same team mapping from the same imagery. This differs considerably from both our own results (8-30% overlap, Table 3) and the other inventory comparisons (19-44% overlap). In these cases, the inventories being compared were published by independent research groups and were not only collected by



different mappers without collaboration but were generated from different sets of satellite images. For example, Roback et al.
580 (2018) used Worldview imagery with high spatial resolution but which suffer from severe warping in the Gorkha study area
due to the steep landscape and oblique look angles (Williams et al., 2018). Even if landslides were correctly identified in both
sets of imagery, differences between inventories could be introduced during georeferencing. These differences could then be
minimised with improved georeferencing though this itself is a difficult problem (Verykokou and Ioannidis, 2018). Figure 8
shows evidence of the same problem for the Wenchuan inventories, where two sets of mapped landslides with strikingly similar
585 patterns are offset by ~1 km. These georeferencing errors are difficult to attribute to a single inventory and appear to vary in
magnitude and direction even over quite short length scales within an inventory (Figures 2 and 8). Thus, improved performance
of ALDI relative to a particular inventory reflects an improved overall workflow rather than specifically the ability to identify
landslides in images.

5.3 Both agreement between manual inventories and ALDI performance differ depending on the property of interest 590 (i.e. spatial agreement, total area, size distribution).

The distinction between the ability of a human mapper to identify a landslide and that of a landslide inventory to identify
whether a particular location is 'landslide affected' is important both for the debate around performance of machine vs. human
vision and because some inventory properties (e.g., total landslide affected area or landslide size-frequency distribution), which
are less sensitive to georeferencing error might not be affected in the same way. Disagreements in landslide size-frequency
595 distributions for manually mapped inventories have already been reported, with most pronounced differences being in roll-
over location, and are usually ascribed to differences in image resolution (Galli et al., 2008; Fan et al., 2019; Tanyas et al.,
2019).

There are, however, a number of applications in which the specific location of the landslide in geographic space is critical
(e.g., landslide susceptibility modelling and hazard mapping). Our results suggest that for the majority of our case studies, the
600 classifier-derived landslide inventory would be a more appropriate product to use in these cases. ALDI is better than at least
one of the inventories in four of the five case studies (though which one is unclear). In the absence of information on which
manual inventory is more accurate, the classifier-derived inventory can be considered the best available dataset (in terms of
spatially explicit classification).

Even in the case of susceptibility mapping, the impact of discrepancy between inventories may be less severe than the direct
605 pixel-based comparison suggests. Sensitivity analyses for a range of locations and of landslide hazard and susceptibility models
indicate that both the statistics of key causative factors (Milledge et al., 2019) and the resultant hazard maps (Ardizzone et al,
2002) remain remarkably consistent between inventories despite considerable locational mismatch (i.e. <50% overlap between
inventories).



5.4 Limitations to ALDI performance

610 ALDI performance varies from site to site, with particularly good performances for Aisen and Gorkha, but particularly poor
for Haiti. The overall poor performance for Haiti may reflect the drier conditions in the study area, which promote vegetation
that is more difficult to differentiate from landslide scars or the higher degree of human influence on land cover, relative to
other sites, which may result in more vegetation changes not related to landslides. ALDI can identify landslides only in areas
where they result in a change in NDVI and will perform better in areas where this change is more pronounced (all else being
615 equal). This will occur where pre-event NDVI is higher due to denser and/or more vigorous vegetation coverage, both of which
result in a larger share of reflectance from leaves, with their more pronounced ‘red edge’ (the red to near infra-red reflectance
change). Conversely, ALDI will likely perform poorly in areas with sparse vegetation such as the epicentral area of the 2010
Sierra Cucapah earthquake (Barlow et al., 2015).

Poor performance for Haiti in comparison with the manual mapping may be due to ALDI’s coarse 30 m resolution relative to
620 the dimensions of the landslides in the study area. ALDI will identify a pixel as landslide affected only if the landslide occupies
enough of the pixel to alter its spectral response, and will perform better when landslides occupy entire pixels, either because
landslide boundaries coincidentally align with pixel boundaries or because landslides are large enough to occupy multiple
pixels. Given their elongate shape (Taylor et al., 2018), landslides with widths <30 m and areas $<2,700$ m² (assuming $L/W=3$,
75th percentile from Taylor et al., 2018) will be partially censored, with the degree of censoring increasing as width declines.
625 Median landslide area in the inventories examined here ranges from 250 m² for Haiti (Harp et al., 2016) to 19,000 m² for
Kashmir (Basharat et al., 2016), with medians less than 2,700 m² in 4 of 14 inventories. Therefore, this censoring will strongly
affect ALDI-derived inventories, particularly in areas with lower relief (such as Haiti), where smaller landslides are expected
to be more common (Jeandet et al., 2019).

Finally, poor performance for Haiti is also likely to reflect the limited number and quality of Landsat images acquired over the
630 study area in the study period. ALDI used imagery from 2005-12 to identify landslides triggered by the Haiti earthquake and
thus relies exclusively on Landsat 5 and 7 data (Landsat 8 launched in 2013). Both Landsat 5 and 7 are problematic for this
study site and period. All the Landsat 7 data contain data gaps due to Scan Line Corrector (SLC) failure from June 2003
onwards and only small amounts of Landsat 5 data for areas outside the USA were retained during this period, limiting archival
imagery in some areas (see Figure S5 in Pekel et al., 2015). For Haiti the pre-earthquake stack is composed of 6 Landsat 5
635 images and 205 Landsat 7 images and the post-earthquake stack of 16 and 91 images, respectively. Limited availability of
Landsat 5 data at this site means that in some areas the classifier relies exclusively on Landsat 7 and is thus unable to calculate
an ALDI value for pixels within the data gaps (these are visible as white stripes in the eastern half of Figure 9b). While some
areas of high ALDI values show good agreement with mapped landslides, there are also large patches of high ALDI values
with complex shapes that are uncharacteristic of landslides and that manual mapping shows as likely false positives (Figure
640 9c).



Given these limitations to Landsat 5 and 7 derived imagery, it is perhaps surprising that ALDI performs so well in the Aisen case (where the stack extends from 2002-2009). This is likely due to the larger number of Landsat 5 images available for the study site (140 in the pre-earthquake stack and 46 in the post-earthquake stack) and to the location of the area of densest landsliding near the centre of a Landsat 7 image where data gaps related to SLC failure are minimised. The 2015 Gorkha earthquake is the only case study for which Landsat 8 data were available perhaps explaining the relatively good performance at this site and offering hope for application to more recent events.

Sparse image data (associated with incomplete archiving of Landsat 5) and sensor problems (primarily SLC failure on Landsat 7) from 2003-2014 suggest ALDI-based mapping in this period should be handled with care. However, the majority of our test earthquakes come from this period and we have demonstrated that even with these constraints, ALDI performs well for four of the five case studies both in absolute terms and relative to manual mapping. However, the Haiti case indicates that ALDI-derived landslide classification cannot be uncritically accepted. This does not necessitate extensive manual mapping but could entail careful checking of the numbers of images in the pre- and post-earthquake stacks, the extent of Landsat 7-derived striping in the ALDI map, and the size and shape of the landslides in the ALDI-derived inventory. Small image stacks (particularly for Landsat 5), extensive striping, and large complex landslide shapes should all be treated as indicators of potentially poor ALDI performance. However, even when large image stacks are available for an earthquake-affected area, cloud cover can limit the number of usable observations per pixel within the pre- and post-earthquake stacks.

ALDI can identify landslide-affected pixels with a high degree of skill (comparable to manual mapping) but is less skilful in identifying discrete landslides, as demonstrated by the difference in ALDI and manually mapped size distributions. As with Parker et al. (2011), additional steps are required to identify separate landslides (e.g., Marc et al., 2016). Calibration based on a small subset of manually mapped landslides followed by subsequent manual editing to remove false positives could result in a very good inventory in a fraction of the time associated with full manual mapping.

5.5 Application of ALDI to future earthquakes

Increased frequency and quality of optical imagery suggests that ALDI should perform well for future earthquakes. In particular, Sentinel 2 imagery can generate NDVI at 10 m spatial resolution (Table 1). The two Sentinel 2 satellites were launched between June 2015 and March 2017, and thus there is a limited stack of pre- or post-earthquake images available to date. The 2018 Hokkaido earthquake offers the best trade-off to date between pre- and post-event data, with a three-year pre-event stack and a one-year post-event stack. As a test of the wider applicability of ALDI to future events, we ran ALDI using the global parameter set identified above, and evaluated its results against landslides mapped from aerial imagery by Wang et al. (2019). The results are extremely promising both at the scale of the entire epicentral area (Figure 9d and e), and of individual landslides, with few false positives, a large area under the ROC curve (0.94), and many landslides clearly delineated by a sharp break from high to low ALDI values (Figure 9f).



6 Conclusion

Rapid derivation of landslide inventories after large triggering events remains a key research challenge. We have developed a parsimonious automatic landslide classifier, ALDI, that uses pre- and post-event stacks of freely-available medium-resolution satellite imagery. We test the classifier against multiple independent manually-mapped inventories from five recent earthquakes. Considering that manually-mapped inventories are typically assumed to be the ‘ground truth’ against which automatic classifiers are evaluated, we find that agreement between different manual inventories is surprisingly low (8-30% of landslide area in common). ALDI often identifies landslides in one inventory missed in the other and even identifies some candidate landslides not in either inventory but that have location and morphometric characteristics that strongly suggest they are true positives.

We further find that ALDI can identify landslide locations with a level of skill that is equal to or better than manual mapping on a pixel by pixel basis. ALDI calibrated to mapped landslides at a site outperforms manual mapping in 10 of 14 cases (i.e. 71%). The only cases where manual mapping performs better are: the two inventories for the 2010 Haiti earthquake, where the stack of available Landsat images is extremely limited; and the cross comparison of Zhang and Watt inventories for the 2015 Gorkha earthquake, where strong agreement between inventories is the result of mapping from very similar satellite imagery.

Even when using a global parameter set, ALDI outperforms manual mapping in 8 of 14 cases (57%) with 10 of 14 cases (71%) either performing better than manual mapping or within the uncertainty in manual mapping performance estimates. These results suggest that ALDI can be applied with considerable confidence to map co-seismic landslides in future earthquakes without the need for additional calibration. Holdback tests do not change either of these statistics and affect both performance metrics by less than 1% (AUC) or two percentage points (TPR_{diff}), suggesting that the set of earthquakes that we have used is large enough to develop a robust global parameter set.

The size distributions for clusters of pixels that are classified as landslides both from manual and automated landslide classification are broadly similar, particularly in their heavy right tail. However, the classifier-derived inventories are fundamentally limited by the resolution of the imagery and their inability to disaggregate amalgamated landslides, so that an object-based approach is required to recover realistic size distributions.

ALDI is fast to run, uses free imagery with near-global coverage and generates landslide information that is of comparable quality to that of costly and time-consuming manual mapping, depending on its intended use. Thus, even in its current form it has the potential to significantly improve the coverage and quantity of landslide inventories. However, its simplicity (performing only pixel-wise analysis) and parsimony of inputs (using only optical imagery) suggests that considerable further improvement should be possible.

Code availability

The Google Earth Engine code to run ALDI will be made available on Github (DavidMilledge/ALDI) on publication.



705 *Data availability.*

All data used in this research is open data. The satellite imagery is provided by USGS and archived by Google within Google Earth Engine. The Watt landslide inventory will be deposited in the USGS open repository of Earthquake-Triggered Ground-Failure Inventories on publication. All other landslide inventories used in this research are already in this repository.

710 *Author contributions.*

J.W. and D.G.M. collected one of the landslide inventories and made it ready for use. D.G.M. designed and implemented the ALDI classifier with input from D.G.B. and analysed data with input from A.L.D.; D.G.M., D.G.B and A.L.D. wrote the paper. A.L.D. organized funds.

715 *Competing interests.* None

Acknowledgements.

Some of this work was undertaken while D.G.M. was supported by the Natural Environment Research Council [grants NE/J01995X/1 and NE/N012216/1]. D.G.B. was supported by a grant from the National Science Foundation (NSF EAR-720 1945431) and by a Gordon and Betty Moore Foundation Data-Driven Discovery Investigator Award (GMBF-4555). We are extremely grateful to Google and the Google Earth Engine team for sharing their software, to the USGS for access to the Landsat data, and to all the research teams involved in the USGS ScienceBase Landslide Inventory project for sharing their landslide inventories.

References

- 725 Aimaiti, Y., Liu, W., Yamazaki, F. and Maruyama, Y., 2019. Earthquake-induced landslide mapping for the 2018 Hokkaido Eastern Iburi earthquake using PALSAR-2 data. *Remote Sensing*, 11(20), p.2351.
- Ardizzone, F., Cardinali, M., Carrara, A., Guzzetti, F. and Reichenbach, P., 2002. Impact of mapping errors on the reliability of landslide hazard maps. *Natural Hazards and Earth System Sciences*, 2, pp.3-14.
- Barlow, J., Martin, Y. and Franklin, S.E., 2003. Detecting translational landslide scars using segmentation of Landsat ETM+ and DEM data in the northern Cascade Mountains, British Columbia. *Canadian Journal of Remote Sensing*, 29(4), pp.510-517.
- 730 Barlow, J., Barisin, I., Rosser, N., Petley, D., Densmore, A. and Wright, T., 2015. Seismically-induced mass movements and volumetric fluxes resulting from the 2010 Mw= 7.2 earthquake in the Sierra Cucapah, Mexico. *Geomorphology*, 230, pp.138-145.
- 735 Barsi, J.A.; Lee, K.; Kvaran, G.; Markham, B.L.; Pedelty, J.A. The spectral response of the Landsat-8 Operational Land Imager. *Remote Sensing*. 2014, 6, 10232-10251. [doi:10.3390/rs61010232](https://doi.org/10.3390/rs61010232)



- Basharat, M., Ali, A., Jadoon, I.A.K., and Rohn, J., 2016, Using PCA in evaluating event-controlling attributes of landsliding in the 2005 Kashmir earthquake region, NW Himalayas, Pakistan: *Natural Hazards*, v. 81, p. 1999-2017, doi: 10.1007/s11069-016-2172-9.
- 740 Basharat, Muhammad, Ali, Abid, Jadoon, I.A.K., Rohn, Joachim, 2017, Landsliding in the 2005 Kashmir earthquake region, NW Himalayas, Pakistan, <https://doi.org/10.5066/F78G8J68>, in Schmitt, R., Tanyas, H., Nowicki Jesse, M.A., Zhu, J., Biegel, K.M., Allstadt, K.E., Jibson, R.W., Thompson, E.M., van Westen, C.J., Sato, H.P., Wald, D.J., Godt, J.W., Gorum, T., Xu, C., Rathje, E.M., Knudsen, K.L., 2017, An Open Repository of Earthquake-triggered Ground Failure Inventories, U.S. Geological Survey data release collection, accessed January 28 2021, at <https://doi.org/10.5066/F7H70DB4>.
- 745 Behling, R., Roessner, S., Kaufmann, H. and Kleinschmit, B., 2014. Automated spatiotemporal landslide mapping over large areas using rapideye time series data. *Remote Sensing*, 6(9), pp.8026-8055.
- Behling, R., Roessner, S., Golovko, D. and Kleinschmit, B., 2016. Derivation of long-term spatiotemporal landslide activity—A multi-sensor time series approach. *Remote Sensing of Environment*, 186, pp.88-104.
- Beven, K. and Binley, A., 1992. The future of distributed models: model calibration and uncertainty prediction. *Hydrological Processes*, 6(3), pp.279-298.
- 750 Burrows, K., Walters, R.J., Milledge, D., Spaans, K. and Densmore, A.L., 2019. A New Method for Large-Scale Landslide Classification from Satellite Radar. *Remote Sensing*, 11(3), p.237.
- Colwell, J. E. 1974. Vegetation canopy reflectance. *Remote Sensing of Environment*, 3, pp. 175–183, 1974.
- Chander, G., Markham, B.L. and Helder, D.L., 2009. Summary of current radiometric calibration coefficients for Landsat
755 MSS, TM, ETM+, and EO-1 ALI sensors. *Remote Sensing of Environment*, 113(5), pp.893-903.
- Đurić, D., Mladenović, A., Pešić-Georgiadis, M., Marjanović, M. and Abolmasov, B., 2017. Using multiresolution and multitemporal satellite data for post-disaster landslide inventory in the Republic of Serbia. *Landslides*, 14(4), pp.1467-1482.
- Earth Engine, 2021, Simple cloud score, an example of computing a cloud-free composite with L8 by selecting the least-cloudy pixel from the collection. Accessed 28 January 2021 at
760 <https://code.earthengine.google.com/dc5611259d9ccab952526b3c2d05ce07>
- ESA. 2017. Sentinel Online; Radiometric Resolutions. Cited at: <https://earth.esa.int/web/sentinel/user-guides/sentinel-2-msi/resolutions/radiometric>
- Fan, X., Scaringi, G., Domènech, G., Yang, F., Guo, X., Dai, L., He, C., Xu, Q. and Huang, R., 2019. Two multi-temporal datasets that track the enhanced landsliding after the 2008 Wenchuan earthquake. *Earth System Science Data*, 11(1), pp.35-
765 55.
- Froude, M.J. and Petley, D.N., 2018. Global fatal landslide occurrence from 2004 to 2016. *Natural Hazards and Earth System Sciences*, 18(8), pp.2161-2181.
- Galli, M., Ardizzone, F., Cardinali, M., Guzzetti, F. and Reichenbach, P., 2008. Comparing landslide inventory maps. *Geomorphology*, 94(3-4), pp.268-289.
- 770 GEE, 2018. <https://developers.google.com/earth-engine/landsat>. Accessed: 5/9/2018



- Goodwin, N.R., Collett, L.J., Denham, R.J., Flood, N. and Tindall, D., 2013. Cloud and cloud shadow screening across Queensland, Australia: An automated method for Landsat TM/ETM+ time series. *Remote Sensing of Environment*, 134, pp.50-65.
- 775 Gorelick, N., Hancher, M., Dixon, M., Ilyushchenko, S., Thau, D. and Moore, R., 2017. Google Earth Engine: Planetary-scale geospatial analysis for everyone. *Remote Sensing of Environment*, 202, pp.18-27.
- Gorum, T., van Westen, C.J., Korup, O., van der Meijde, M., Fan, X. and van der Meer, F.D., 2013. Complex rupture mechanism and topography control symmetry of mass-wasting pattern, 2010 Haiti earthquake. *Geomorphology*, 184, pp.127-138.
- Gorum, T., Korup, O., van Westen, C.J., van der Meijde, M., Xu, C., and van der Meer, F.D., 2014, Why so few? Landslides 780 triggered by the 2002 Denali earthquake, Alaska. *Quaternary Science Reviews*, v. 95, p. 80-94, doi: 10.1016/j.quascirev.2014.04.032.
- Gorum, Tolga, van Westen, C.J., Korup, Oliver, van der Meijde, Mark, Fan, X., van der Meer, F.D., 2017a, Mass-wasting triggered by the 2010 Haiti earthquake, <https://doi.org/10.5066/F7H130HG>, in Schmitt, R.G., Tanyas, Hakan, Nowicki Jessee, M.A., Zhu, J., Biegel, K.M., Allstadt, K.E., Jibson, R.W., Thompson, E.M., van Westen, C.J., Sato, H.P., Wald, D.J., Godt, 785 J.W., Gorum, Tolga, Xu, Chong, Rathje, E.M., Knudsen, K.L., 2017, An Open Repository of Earthquake-triggered Ground Failure Inventories, U.S. Geological Survey data release collection, accessed January 28 2021, at <https://doi.org/10.5066/F7H70DB4>.
- Gorum, Tolga, Korup, Oliver, van Westen, C. J., van der Meijde, Mark, Xu, Chong, van der Meer, F. D. , 2017b, Landslides triggered by the 2007 M 6.2 Aisen, Chile earthquake , <https://doi.org/10.5066/F7125R5V>, in Schmitt, R.G., Tanyas, Hakan, 790 Nowicki Jessee, M.A., Zhu, J., Biegel, K.M., Allstadt, K.E., Jibson, R.W., Thompson, E.M., van Westen, C.J., Sato, H.P., Wald, D.J., Godt, J.W., Gorum, Tolga, Xu, Chong, Rathje, E.M., Knudsen, K.L., 2017, An Open Repository of Earthquake-triggered Ground Failure Inventories, U.S. Geological Survey data release collection, accessed Jan 28, 2021, at <https://doi.org/10.5066/F7H70DB4>.
- Greenbaum, D., Tutton, M., Bowker, M.R., Browne, T.J., Buleka, J., Grealley, K.B., Kuna, G., McDonald, A.J.W., Marsh, 795 S.H., Northmore, K.H. and O'Connor, E.A., 1995. *Rapid methods of landslide hazard mapping: Papua New Guinea case study*. Technical Report WC/95/27, British Geological Survey (BGS), Natural Environmental Research Council, Keyworth, Nottingham.
- Guzzetti, F., Mondini, A.C., Cardinali, M., Fiorucci, F., Santangelo, M. and Chang, K.T., 2012. Landslide inventory maps: New tools for an old problem. *Earth-Science Reviews*, 112(1-2), pp.42-66.
- 800 Haralick, R.M., and Shapiro, L.G., 1992, *Computer and Robot Vision*, Addison-Wesley, Reading, Mass.
- Harp, E.L., Jibson, R.W. and Schmitt, R.G., 2016. Map of landslides triggered by the January 12, 2010, Haiti earthquake. *US Geological Survey Scientific Investigations Map*, 3353, p.15.
- Harp, E.L., Jibson, R.W., Schmitt, R.G., 2017, Map of landslides triggered by the January 12, 2010, Haiti earthquake, <https://doi.org/10.5066/F7C827SR>, in Schmitt, R.G., Tanyas, Hakan, Nowicki Jessee, M.A., Zhu, J., Biegel, K.M., Allstadt,



- 805 K.E., Jibson, R.W., Thompson, E.M., van Westen, C.J., Sato, H.P., Wald, D.J., Godt, J.W., Gorum, Tolga, Xu, Chong, Rathje, E.M., Knudsen, K.L., 2017, An Open Repository of Earthquake-triggered Ground Failure Inventories, U.S. Geological Survey data release collection, accessed January 28 2021, at <https://doi.org/10.5066/F7H70DB4>.
- Hilton, R.G., Galy, A., Hovius, N., Chen, M.C., Horng, M.J. and Chen, H., 2008. Tropical-cyclone-driven erosion of the terrestrial biosphere from mountains. *Nature Geoscience*, 1(11), pp.759-762.
- 810 Irish, R.R., 2000. Landsat 7 automatic cloud cover assessment. In *Algorithms for Multispectral, Hyperspectral, and Ultraspectral Imagery VI* (Vol. 4049, pp. 348-355). International Society for Optics and Photonics.
- Jeandet, L., Steer, P., Lague, D. and Davy, P., 2019. Coulomb mechanics and relief constraints explain landslide size distribution. *Geophysical Research Letters*, 46(8), pp.4258-4266.
- Konishi, T. and Suga, Y., 2018. Landslide detection using COSMO-SkyMed images: a case study of a landslide event on Kii Peninsula, Japan. *European Journal of Remote Sensing*, 51(1), pp.205-221.
- 815 Li, G., West, A.J., Densmore, A.L., Jin, Z., Parker, R.N. and Hilton, R.G., 2014. Seismic mountain building: Landslides associated with the 2008 Wenchuan earthquake in the context of a generalized model for earthquake volume balance. *Geochemistry, Geophysics, Geosystems*, 15(4), pp.833-844.
- Li, Gen, West, A.J., Densmore, A.L., Jin, Zhangdong, Parker, R.N., Hilton, R.G., 2017, Landslides associated with the 2008
- 820 Wenchuan earthquake, <https://doi.org/10.5066/F7MS3R8Z>, in Schmitt, R.G., Tanyas, Hakan, Nowicki Jessee, M.A., Zhu, J., Biegel, K.M., Allstadt, K.E., Jibson, R.W., Thompson, E.M., van Westen, C.J., Sato, H.P., Wald, D.J., Godt, J.W., Gorum, Tolga, Xu, Chong, Rathje, E.M., Knudsen, K.L., 2017, An Open Repository of Earthquake-triggered Ground Failure Inventories, U.S. Geological Survey data release collection, accessed January 28 2021, at <https://doi.org/10.5066/F7H70DB4>.
- Marano, K.D., Wald, D.J. and Allen, T.I., 2010. Global earthquake casualties due to secondary effects: a quantitative analysis
- 825 for improving rapid loss analyses. *Natural Hazards*, 52(2), pp.319-328.
- Marc, O., Hovius, N., Meunier, P., Uchida, T. and Hayashi, S., 2015. Transient changes of landslide rates after earthquakes. *Geology*, 43(10), pp.883-886.
- Marc, O., Hovius, N., Meunier, P., Gorum, T. and Uchida, T., 2016. A seismologically consistent expression for the total area and volume of earthquake-triggered landsliding. *Journal of Geophysical Research: Earth Surface*, 121(4), pp.640-663.
- 830 Martin, Y.E. and Franklin, S.E., 2005. Classification of soil-and bedrock-dominated landslides in British Columbia using segmentation of satellite imagery and DEM data. *International Journal of Remote Sensing*, 26(7), pp.1505-1509.
- Milledge, D.G., Densmore, A.L., Bellugi, D., Rosser, N.J., Watt, J., Li, G. and Oven, K.J., 2019. Simple rules to minimise exposure to coseismic landslide hazard. *Natural Hazards and Earth System Sciences*, 19(4), pp.837-856.
- Marc, O., Behling, R., Andermann, C., Turowski, J.M., Illien, L., Roessner, S. and Hovius, N., 2019. Long-term erosion of
- 835 the Nepal Himalayas by bedrock landsliding: the role of monsoons, earthquakes and giant landslides. *Earth Surface Dynamics*, 7(1), pp.107-128.
- Mondini, A.C., Santangelo, M., Rocchetti, M., Rossetto, E., Manconi, A. and Monserrat, O., 2019. Sentinel-1 SAR amplitude imagery for rapid landslide detection. *Remote Sensing*, 11(7), p.760.



- Parker, R.N., Densmore, A.L., Rosser, N.J., De Michele, M., Li, Y., Huang, R., Whadcoat, S. and Petley, D.N., 2011. Mass wasting triggered by the 2008 Wenchuan earthquake is greater than orogenic growth. *Nature Geoscience*, 4(7), p.449.
- Pawłuszek, K., Borkowski, A. and Tarolli, P., 2017. Towards the optimal pixel size of DEM for automatic mapping of landslide areas. *International Archives of the Photogrammetry, Remote Sensing & Spatial Information Sciences*, 42.
- Pekel, J.F., Cottam, A., Gorelick, N. and Belward, A.S., 2016. High-resolution mapping of global surface water and its long-term changes. *Nature*, 540(7633), p.418. <https://www.nature.com/articles/nature20584/figures/5>
- 845 Reichenbach, P., Rossi, M., Malamud, B.D., Mihir, M. and Guzzetti, F., 2018. A review of statistically-based landslide susceptibility models. *Earth-Science Reviews*, 180, pp.60-91.
- Roback, Kevin, Clark, M.K., West, A.J., Zekkos, Dimitrios, Li, Gen, Gallen, S.F., Champlain, Deepak, and Godt, J.W., 2017, Map data of landslides triggered by the 25 April 2015 Mw 7.8 Gorkha, Nepal earthquake: U.S. Geological Survey data release, <https://doi.org/10.5066/F7DZ06F9>.
- 850 Roback, K., Clark, M.K., West, A.J., Zekkos, D., Li, G., Gallen, S.F., Champlain, D. and Godt, J.W., 2018. The size, distribution, and mobility of landslides caused by the 2015 Mw7. 8 Gorkha earthquake, Nepal. *Geomorphology*, 301, pp.121-138.
- Robinson, T.R., Rosser, N. and Walters, R.J., 2019. The spatial and temporal influence of cloud cover on satellite-based emergency mapping of earthquake disasters. *Scientific Reports*, 9(1), pp.1-9.
- 855 Santangelo, M., Marchesini, I., Bucci, F., Cardinali, M., Fiorucci, F. and Guzzetti, F., 2015. An approach to reduce mapping errors in the production of landslide inventory maps. *Natural Hazards and Earth System Sciences*, 15(9).
- Sauchyn, D.J. and Trench, N.R., 1978. Landsat applied to landslide mapping. *Photogrammetric Engineering and Remote Sensing*, 44(6).
- Sato, H.P., Hasegawa, H., Fujiwara, S., Tobita, M., Koarai, M., Une, H. and Iwahashi, J., 2007. Interpretation of landslide distribution triggered by the 2005 Northern Pakistan earthquake using SPOT 5 imagery. *Landslides*, 4(2), pp.113-122.
- 860 Sato, H.P., Hasegawa, Hiroyuki, Fujiwara, Satoshi, Tobita, Mikio, Koarai, Mamoru, Une, Hiroshi, Iwahashi, Junko , 2017, Landslide distribution triggered by the 2005 Northern Pakistan earthquake using SPOT 5 imagery, <https://doi.org/10.5066/F7SJ1J42>, in Schmitt, R.G., Tanyas, Hakan, Nowicki Jesse, M.A., Zhu, J., Biegel, K.M., Allstadt, K.E., Jibson, R.W., Thompson, E.M., van Westen, C.J., Sato, H.P., Wald, D.J., Godt, J.W., Gorum, Tolga, Xu, Chong, Rathje, E.M., Knudsen, K.L., 2017, An Open Repository of Earthquake-triggered Ground Failure Inventories, U.S. Geological Survey data release collection, accessed January 28 2021, at <https://doi.org/10.5066/F7H70DB4>.
- 865 Scheip, C.M. and Wegmann, K.W., 2021. HazMapper: a global open-source natural hazard mapping application in Google Earth Engine. *Natural Hazards and Earth System Sciences*, 21(5), pp.1495-1511.
- Science Base Community, 2021, Science base open repository of landslide inventories, accessed January 28 2021, at <https://www.sciencebase.gov/catalog/item/586d824ce4b0f5ce109fc9a6>.
- 870 Sepulveda, S., A. Serey, M. Lara, A. Pavez, and S. Rebolledo (2010a), Landslides induced by the April 2007 Aisen Fjord earthquake, Chilean Patagonia, *Landslides*, 7(4), 483-492, doi:10.1007/s10346-010-0203-2



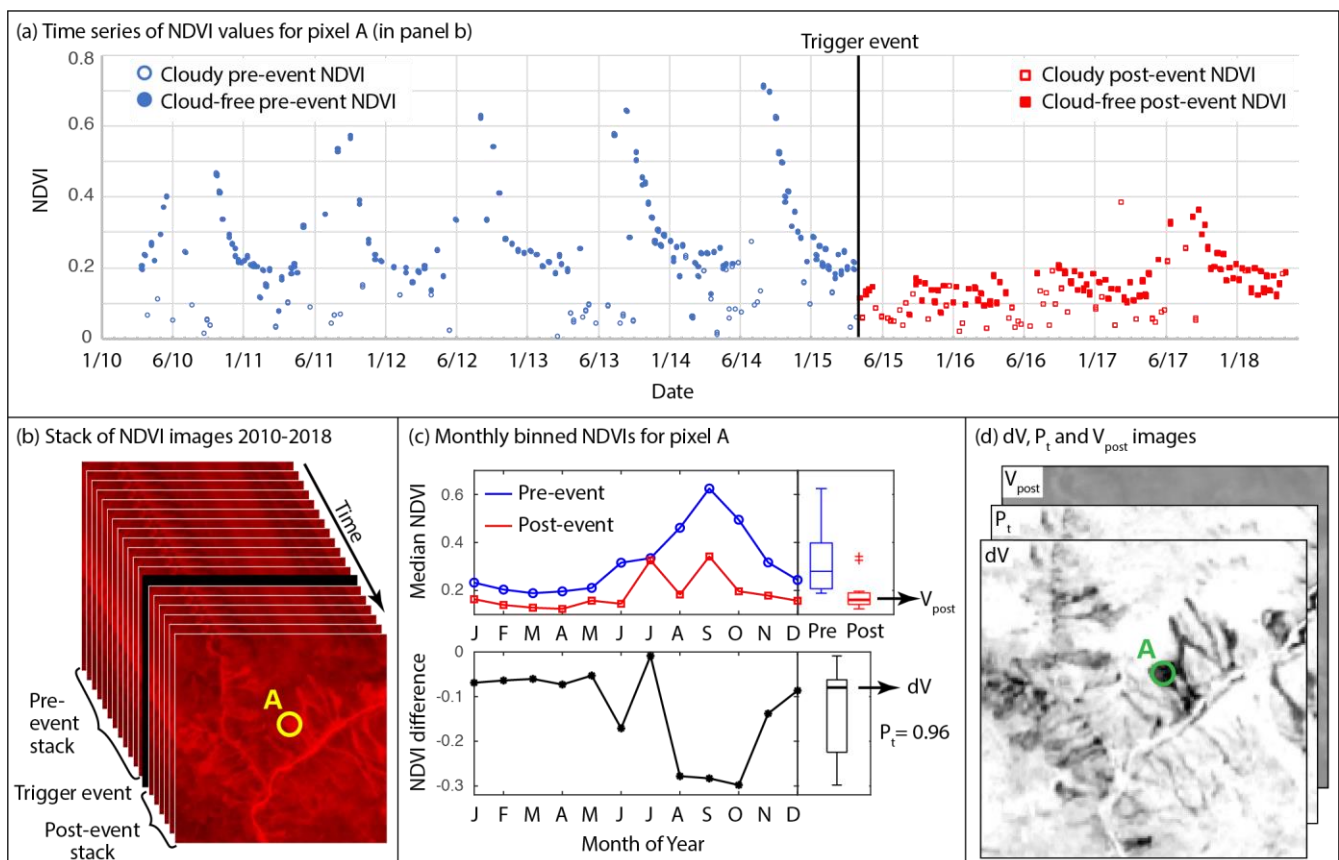
- Sepulveda, S., Serey, A., Lara, M., Pavez, A., Rebolledo, S., 2010b, Landslides induced by the April 2007 Aisen Fjord earthquake, Chilean Patagonia, <https://doi.org/10.5066/P943ID6R>, in Schmitt, R., Tanyas, H., Jessee, M.A., Zhu, J., Biegel, K., Allstadt, K.E., Jibson, R.W., Thompson, E.M., van Westen, C., Sato, H.P., Wald, D.J., Godt, J.W., Gorum, T., Moss, R.E.S., Xu, C., Rathje, E.M., Knudsen, K.L., 2017, An Open Repository of Earthquake-triggered Ground Failure Inventories, U.S. Geological Survey data release collection, accessed January 28 2021, at <https://doi.org/10.5066/F7H70DB4>
- 875 Swamidass, S.J., Azencott, C.A., Daily, K. and Baldi, P., 2010. A CROC stronger than ROC: measuring, visualizing and optimizing early retrieval. *Bioinformatics*, 26(10), pp.1348-1356.
- 880 Tanyaş, H., Van Westen, C.J., Allstadt, K.E., Anna Nowicki Jessee, M., Görüm, T., Jibson, R.W., Godt, J.W., Sato, H.P., Schmitt, R.G., Marc, O. and Hovius, N., 2017. Presentation and analysis of a worldwide database of earthquake-induced landslide inventories. *Journal of Geophysical Research: Earth Surface*, 122(10), pp.1991-2015.
- Tanyaş, H., van Westen, C.J., Allstadt, K.E. and Jibson, R.W., 2019. Factors controlling landslide frequency–area distributions. *Earth Surface Processes and Landforms*, 44(4), pp.900-917.
- 885 Taylor, F.E., Malamud, B.D., Witt, A. and Guzzetti, F., 2018. Landslide shape, ellipticity and length-to-width ratios. *Earth Surface Processes and Landforms*, 43(15), pp.3164-3189.
- Tucker, C. J. 1979. Red and photographic infrared linear combinations for monitoring vegetation. *Remote Sensing of Environment*, 8, pp. 127–150.
- Van Westen, C.J., Van Asch, T.W. and Soeters, R., 2006. Landslide hazard and risk zonation—why is it still so difficult? *Bulletin of Engineering Geology and the Environment*, 65(2), pp.167-184.
- Verykokou, S. and Ioannidis, C., 2018. Oblique aerial images: a review focusing on georeferencing procedures. *International Journal of Remote Sensing*, 39(11), pp.3452-3496.
- Wang, F., Fan, X., Yunus, A.P., Subramanian, S.S., Alonso-Rodriguez, A., Dai, L., Xu, Q. and Huang, R., 2019. Coseismic landslides triggered by the 2018 Hokkaido, Japan (M w 6.6), earthquake: spatial distribution, controlling factors, and possible failure mechanism. *Landslides*, 16(8), pp.1551-1566.
- 895 Watt, J., 2016. *The characteristics of coseismic landslides triggered by the 2015 Gorkha earthquake*. Undergraduate Dissertation, Durham University
- Williams, J.G., Rosser, N.J., Kincey, M.E., Benjamin, J., Oven, K.J., Densmore, A.L., Milledge, D.G., Robinson, T.R., Jordan, C.A. and Dijkstra, T.A., 2018. Satellite-based emergency mapping using optical imagery: experience and reflections from the 2015 Nepal earthquakes. *Natural Hazards and Earth System Sciences*, 18, pp.185-205.
- 900 Xu, C., Xu, X., Yao, X., and Dai, F., 2014, Three (nearly) complete inventories of landslides triggered by the May 12, 2008 Wenchuan Mw 7.9 earthquake of China and their spatial distribution statistical analysis: *Landslides*, 11(3), p. 441-461, doi: 10.1007/s10346-013-0404-6.
- Xu, Chong, Xu, Xiwei, Yao, Xin, Dai, Fuchu, 2017, Landslides triggered by the May 12, 2008, Wenchuan Mw 7.9 earthquake of China, <https://doi.org/10.5066/F7RJ4H0P>, in Schmitt, R.G., Tanyas, Hakan, Nowicki Jessee, M.A., Zhu, J., Biegel, K.M., Allstadt, K.E., Jibson, R.W., Thompson, E.M., van Westen, C.J., Sato, H.P., Wald, D.J., Godt, J.W., Gorum, Tolga, Xu, Chong,
- 905



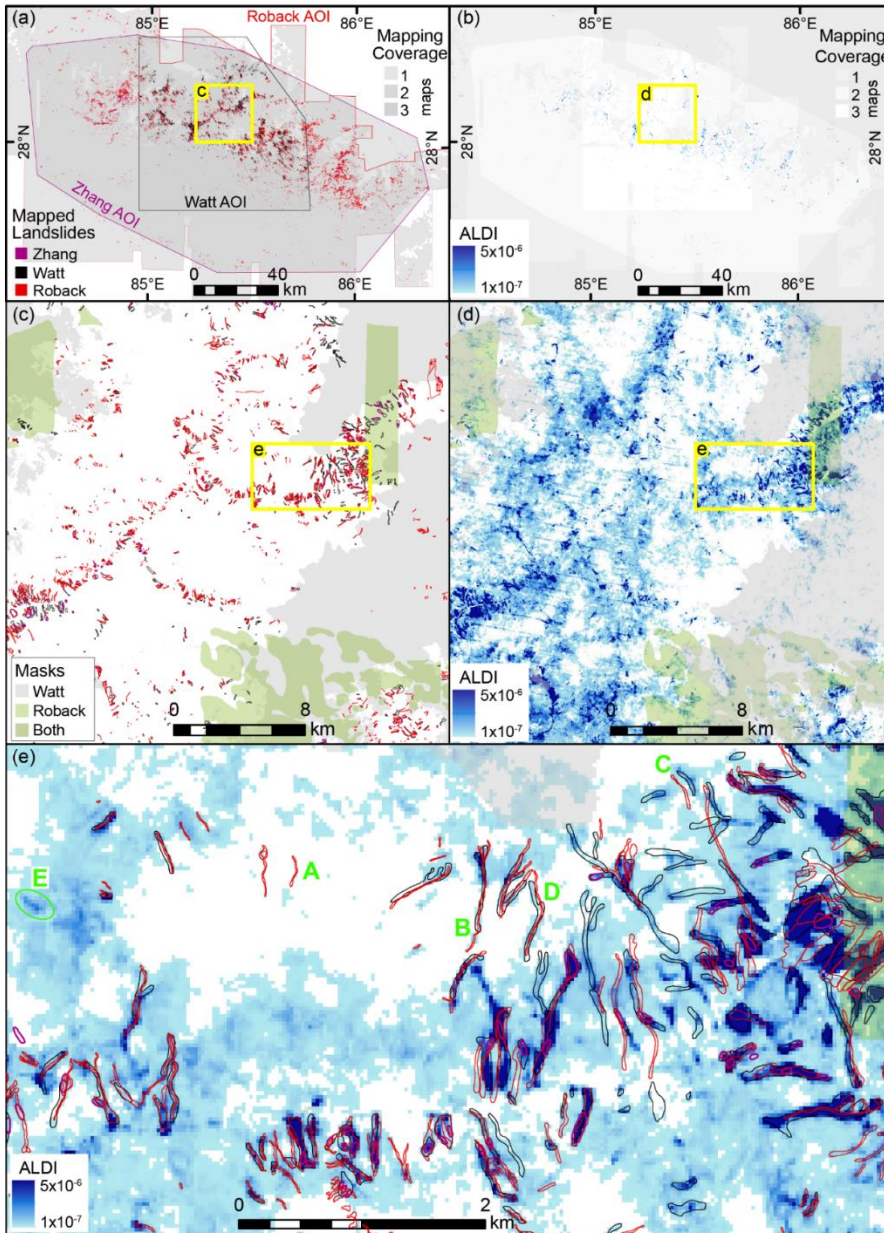
Rathje, E.M., Knudsen, K.L., 2017, An Open Repository of Earthquake-triggered Ground Failure Inventories, U.S. Geological Survey data release collection, accessed January 28 2021, at <https://doi.org/10.5066/F7H70DB4>.

Zhang, J.Q., Liu, R.K., Deng, W., Khanal, N.R., Gurung, D.R., Murthy, M.S.R. and Wahid, S., 2016. Characteristics of
 910 landslide in Koshi River basin, central Himalaya. *Journal of Mountain Science*, 13(10), pp.1711-1722.

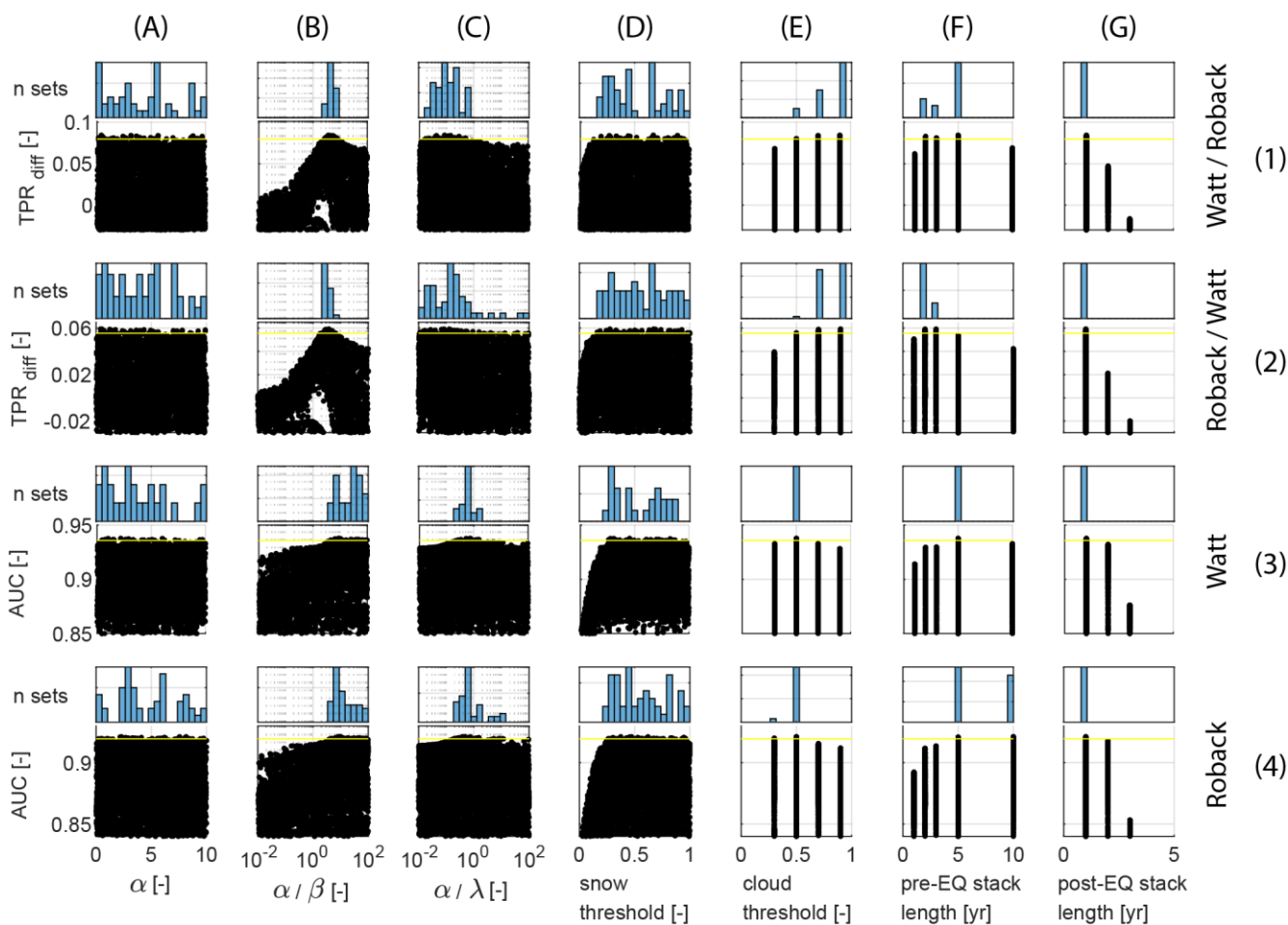
Zhang, Jian-qiang, Liu, Rong-kun, Deng, Wei, Khanal, N.R., Gurung, D.R., Murthy, M.S.R., and Wahid, S., 2017, Characteristics of landslides in Koshi River basin, Central Himalaya, <https://doi.org/10.5066/F73T9FQ1>, in Schmitt, R.G., Tanyas, Hakan, Nowicki Jesse, M.A., Zhu, J., Biegel, K.M., Allstadt, K.E., Jibson, R.W., Thompson, E.M., van Westen, C.J., Sato, H.P., Wald, D.J., Godt, J.W., Gorum, Tolga, Xu, Chong, Rathje, E.M., Knudsen, K.L., 2017, An Open Repository of
 915 Earthquake-triggered Ground Failure Inventories, U.S. Geological Survey data release collection, accessed January 28 2021, at <https://doi.org/10.5066/F7H70DB4>.



920 **Figure 1: ALDI pre-processing steps.** (a) Time series of NDVI values for a landslide-affected pixel (circled in panels b and d) before and after the trigger event, with cloud-free values shown as solid symbols. This time series is derived from a stack of NDVI images (b) and is used to calculate monthly median NDVI before and after the earthquake and their difference (c), which can be used to calculate dV , P_t and V_{post} for every pixel in the study area (d).



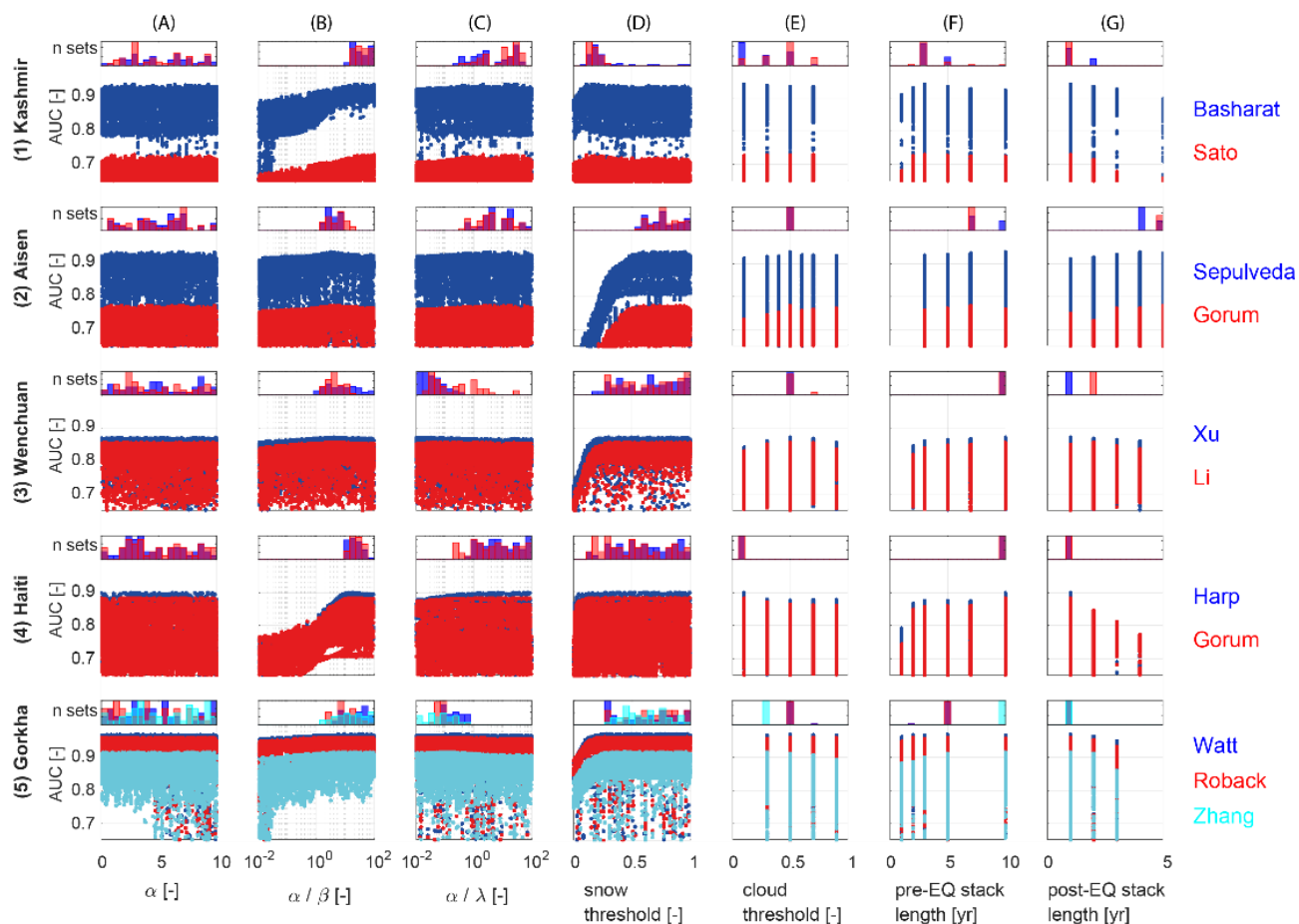
925 Figure 2: Mapped landslides and the ALDI classifier for the Gorkha study site. a) Mapped landslides at the scale of the full study
area with AOIs (the mapped area) shown in grey. Zhang refers to the inventory of Zhang et al. (2016), Roback to the inventory of
Roback et al. (2018), and Watt to the inventory of Watt (2016). The yellow box shows the location of panels (b) and (c); b) ALDI
values for the full study area with areas outside the AOI in grey; c) mapped landslides from the three inventories for a subset of the
study area, with unmapped areas (masks) shaded green and grey (no mask was reported for Zhang et al., 2016). The yellow box
930 shows the location of panel (e); d) ALDI values for the same subset of the study area shown in (c); e) detailed view of mapped
landslides from the three inventories and ALDI values. Green labels indicate examples of: A) missed landslides, B) agreement
between inventories, C) offset landslide outlines, D) warped landslide outlines, and E) landslides identified by ALDI but missed by
manual mapping. None of the study area was masked in the mapping of Zhang et al. (2016).



935

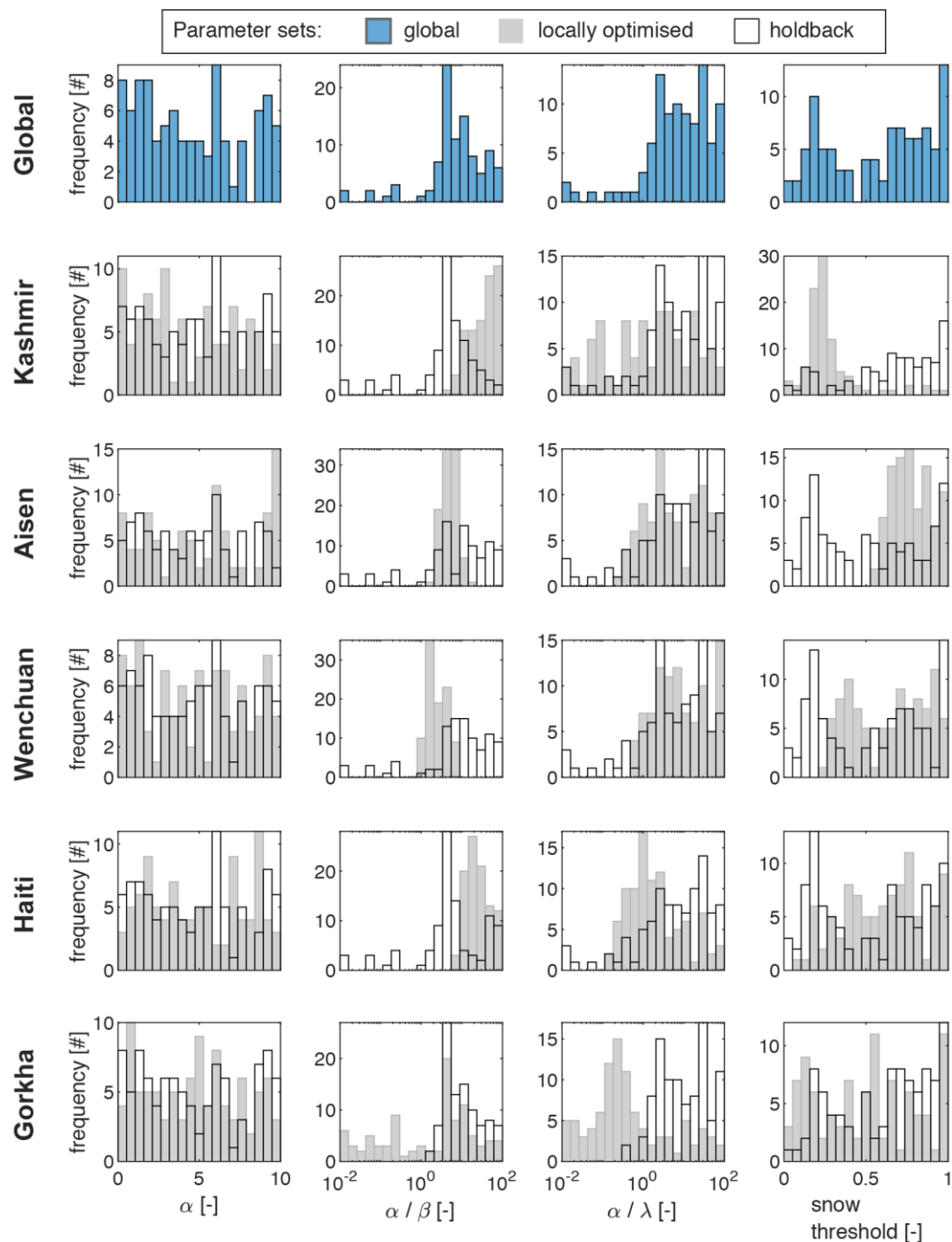
940

Figure 3: Dotty plots and posterior parameter distributions for the Gorkha case study for the seven tuneable parameters associated with ALDI (columns) evaluated using two of the test datasets (Watt and Roback) and two performance metrics (rows): TPR_{diff} , the difference in TPR between ALDI and the competitor inventory at the FPR defined by the competitor inventory; and AUC, the area under the ROC curve, a more general indicator of classifier performance over the full range of FPRs. ‘Watt/Roback’ refers to using Watt as the check dataset and Roback as the competitor in row 1; ‘Roback/Watt’ refers to the converse in row 2. Watt is used as the check dataset in row 3, and Roback as the check dataset in row 4. Points plotting above the yellow line are results for the best 100 parameter values. In each case the parameter distributions are for the best 100 parameter sets evaluated using the same metric and datasets as the dotty plot below it. Dotty plots for the other Gorkha inventories and for all other sites are given in the Supplementary Information.



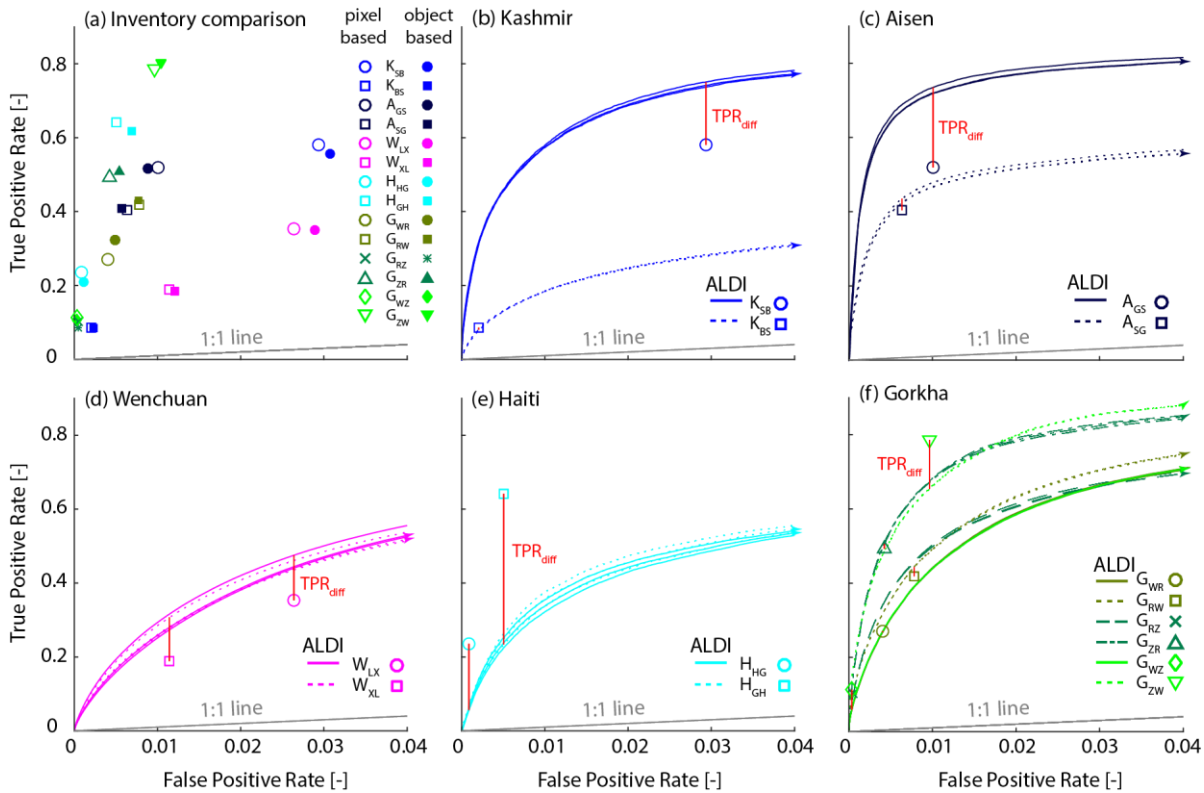
945

Figure 4: Dotty plots and posterior parameter distributions for the seven tuneable parameters associated with ALDI (columns A-G) for the five study earthquakes (rows 1-5). Dotty plots show classifier performance evaluated using AUC, the area under the ROC curve. Blue or red colours indicate the inventory used as the check dataset, as shown to the right. Parameter distributions are for the best 100 parameter sets evaluated using the same metric.



950

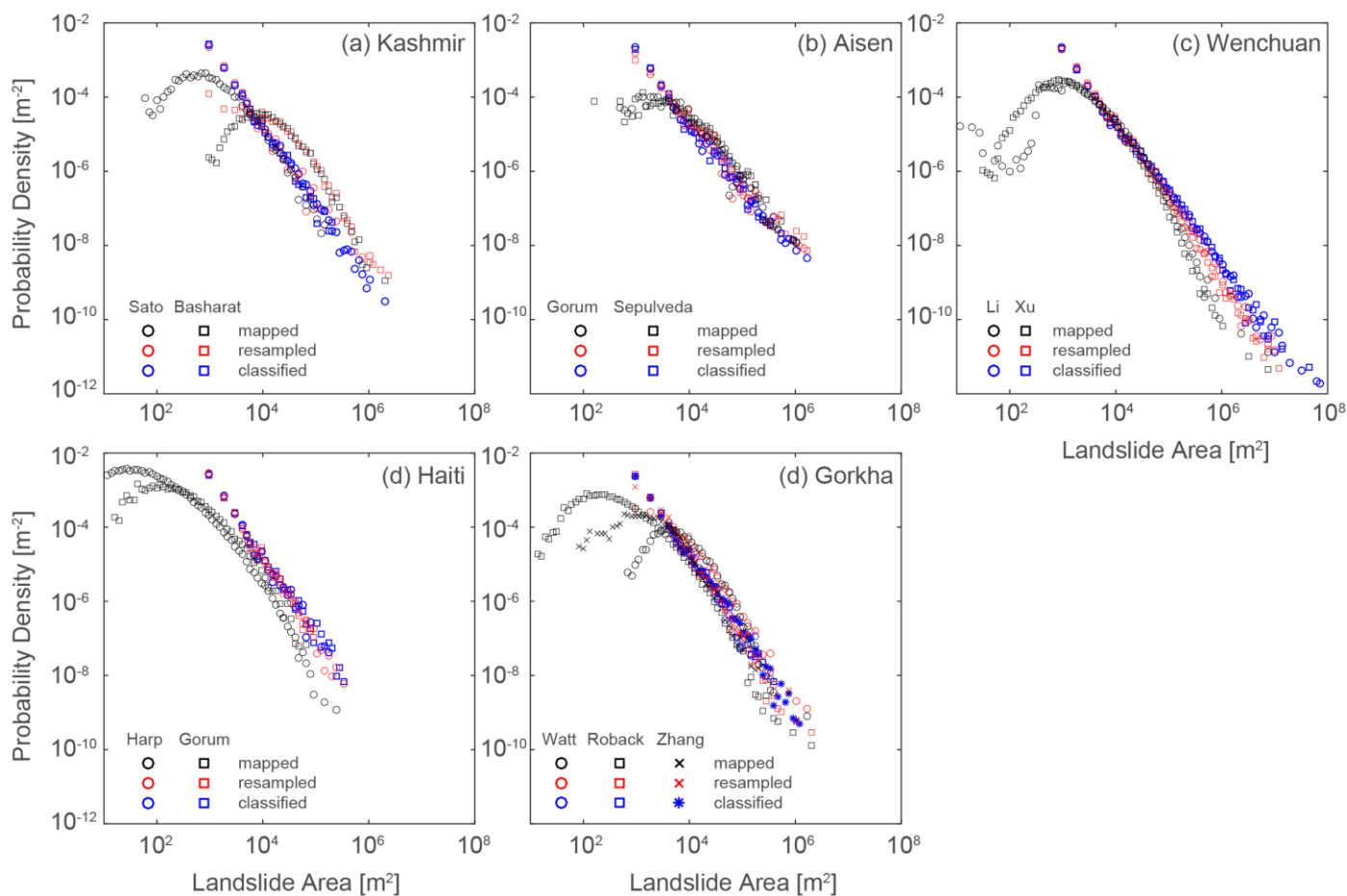
Figure 5: Posterior parameter distributions for the four parameters external to Google Earth Engine after global optimisation (top row) and local optimisation for each earthquake. Rows 2-5 show posterior frequency distributions for each ALDI parameter following local optimisation (grey bars) and the holdback parameter set derived from the global set excluding locally optimised parameters (hollow bars).



955

960

Figure 6: a) TPR, FPR pairs for the 14 inventory cross comparisons. Open symbols are calculated from a pixel-based analysis at 30 m resolution, solid symbols are calculated from an object-based analysis using mapped polygons. The grey line shows the naïve (random) 1:1 relationship. Note difference in x- and y-axis scales for this and all other panels; b)-f) ROC curves for ALDI for each case study. There are three ROC curves for ALDI evaluated against each check inventory (e.g., K_{SB}) all with the same line style (solid or dashed). In every case the upper curve is from ALDI with locally optimised parameters, the middle curve (indicated with an arrowed end) is from ALDI with global parameters and the lower curve is from ALDI with holdback parameters. The global and holdback curves are indistinguishable in almost all cases. Red lines indicate the value of TPR_{diff} , the difference in TPR between ALDI and the competitor inventory when both are evaluated using the same check inventory. Legend acronyms indicate the study site (e.g., K) with the check and then competitor inventory labels as subscripts; see Table 3.



965

Figure 7: Empirical size distributions for manually mapped and classified landslides for the five case studies. Manually mapped pdfs are calculated from areas of mapped polygons, resampled pdfs are calculated from patch areas generated from the mapped polygons resampled to a 30 m grid, and classified pdfs are calculated from clustered pixel areas generated by thresholding the ALDI classification values.

970

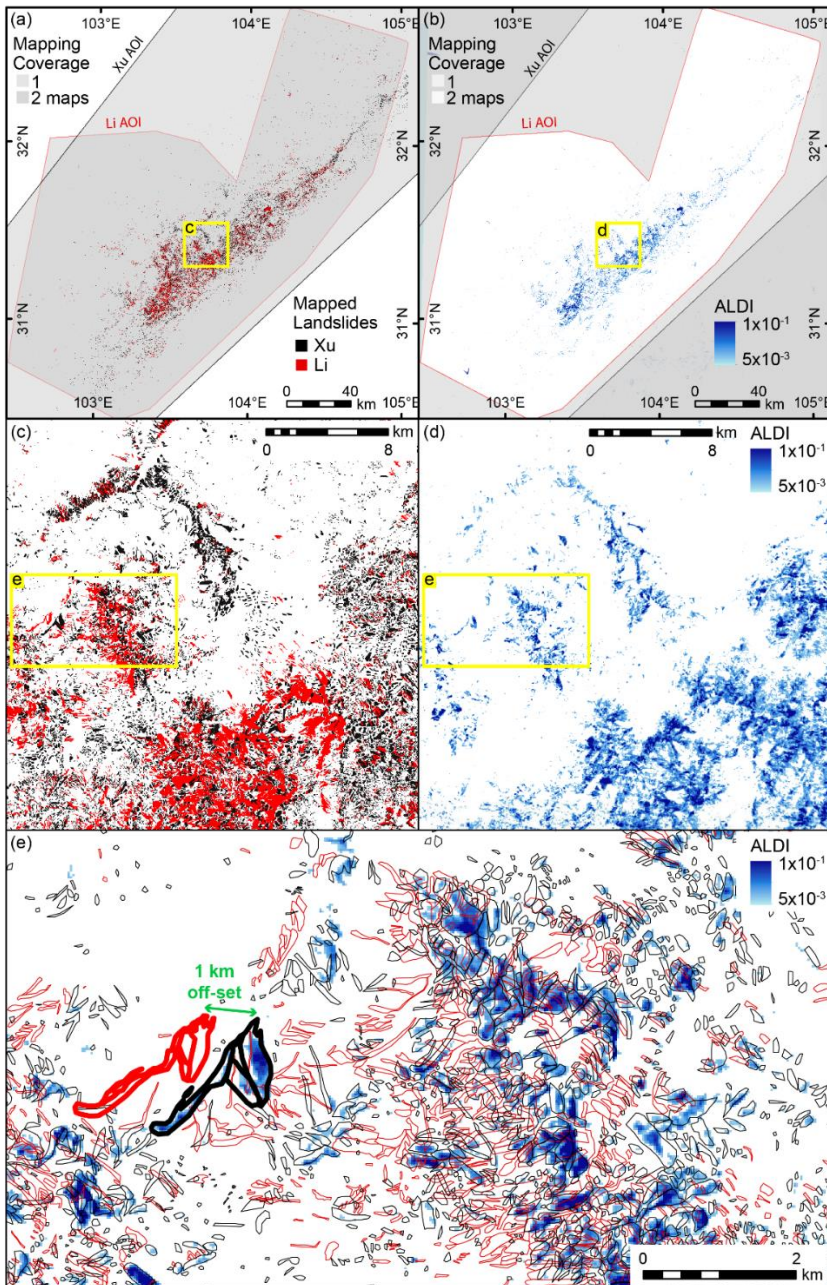
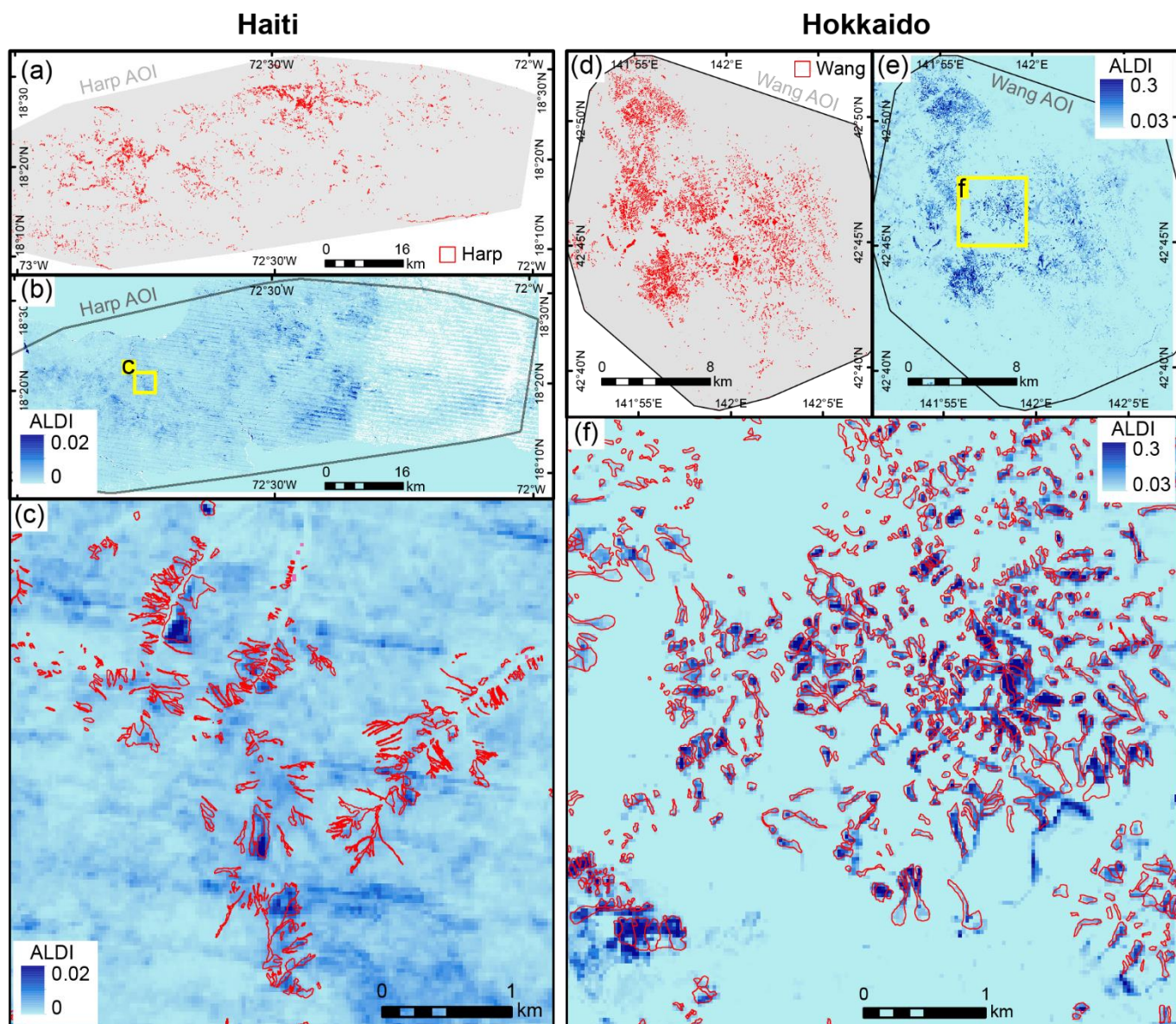


Figure 8: Mapped landslides and ALDI classifier results for the Wenchuan study site. a) Mapped landslides at the scale of the full study area with AOIs shown in grey. Xu refers to the inventory of Xu et al. (2014), and Li to the inventory of Li et al. (2014). The yellow box shows the location of panels (b) and (c); b) ALDI values for the full study area with areas outside the AOI in grey. Color bar shown in panel (e); c) mapped landslides from the two inventories for a subset of the study area. The yellow box shows the location of panel (e); d) ALDI values for the same subset of the study area shown in (c); e) detailed view of mapped landslides from the two inventories and ALDI values. Thicker outlines in (e) indicate landslides of very similar geometry that are offset by ~1 km in the different inventories; the ALDI pattern suggests that the mapping of Xu et al. (2014) is more likely to be correctly georeferenced in this case.

975



980

985

Figure 9: Mapped landslides and the ALDI classifier for the Haiti (left) and Hokkaido (right) study sites. a) Mapped landslides from Harp et al. (2016) in Haiti at the scale of the full study area with the associated AOI shown in grey; b) ALDI values for the full study area, the yellow box shows the location of panel c; c) ALDI values overlain by mapped landslides from Harp et al. (2016) for a subset of the study area; d) Mapped landslides from Wang et al. (2019) in Hokkaido at the scale of the full study area with the associated AOI shown in grey; e) ALDI values for the full study area, the yellow box shows the location of panel f; f) ALDI values overlain by mapped landslides from Wang for a subset of the study area. ALDI uses Landsat 5 and Landsat 7 for Haiti and Sentinel 2 for Hokkaido, both are gridded at 30 m resolution.



Table 1: Landsat and Sentinel image characteristics (Barsi et al., 2014; ESA, 2017b).

	Landsat 5 and 7	Landsat 8	Sentinel 2
Green (μm)	Band 2: 0.52-0.60	Band 3: 0.53-0.59	Band 3: 0.52-0.60
Red (μm)	Band 3: 0.63-0.69	Band 4: 0.64-0.67	Band 4: 0.65-0.69
Near infra-red (μm)	Band 4: 0.77-0.90	Band 5: 0.85-0.88	Band 8: 0.76-0.91
Shortwave infra-red (μm)	Band 5: 1.55-1.75	Band 6: 1.57-1.65	Band 11: 1.51-1.70
Spatial resolution (m)	30	30	10
Revisit time (days)	16	16	5
Operational life	1984-2013 (L5) 1999-present (L7)	2013-present	June 2015-present (S2a) March 2017-present (S2b)

990

Table 2: Parameters for Landsat simple cloudscore, equations 2a-f

Threshold	Minimum	Maximum
Blue (Eqn 2a)	$R_{bmin} = 0.1$	$R_{bmax} = 0.3$
Visible (Eqn 2b)	$R_{vmin} = 0.2$	$R_{vmax} = 0.8$
Infra-red (Eqn 2c)	$R_{irmin} = 0.3$	$R_{irmax} = 0.8$
Temperature (Eqn 2d)	$Temp_{min} = 290$	$Temp_{max} = 300$
NDSI (Eqn 2e)	$NDSI_{min} = 0.6$	$NDSI_{max} = 0.8$



995 **Table 3: Performance metrics for ALDI applied with the different parameter sets to predict landslides from each of the 14 inventory**
pairs. Abbreviated names for the inventory pairs indicate the case study with subscripts denoting first check and then competitor
inventories (e.g., K_{SB} denotes the Kashmir earthquake with Sato as the check inventory and Basharat as the competitor inventory). True
positive rate (TPR) and false positive rate (FPR) are reported for both object-based analysis (in brackets), and pixel-based analysis at 30
m resolution. Overlap indicates the percentage overlap between pairs of landslide inventories. Shading in right hand columns indicates
relative performance within each column (i.e. for that metric and calibration) with linear colour scale from best (blue) to worst (red).
 1000 **Vertical blocks reflect different performance metrics: TPR_{diff} , the percentage difference in TPR between ALDI and the competitor**
inventory when evaluated for that check inventory; and AUC, the area under the ROC curve. Columns within each block reflect different
ALDI calibration strategies: local calibration optimised to both site and check inventory; global calibration using a compilation of the
best parameter sets from all sites; and holdback calibration where parameter sets from the test site are excluded. Note that positive values
of TPR_{diff} reflect cases where ALDI outperforms manual mapping while negative values reflect cases where manual mapping is better.

	Check Inventory	Competitor Inventory	TPR [-]		FPR [-]		Overlap [%]	TPR _{diff} [%]			AUC [-]			
			Pixel-based (Object-based)	Pixel-based (Object-based)	Pixel-based (Object-based)	Pixel-based (Object-based)		Local	Global	Holdback	Local	Global	Holdback	
Kashmir (K)														
	(K_{SB}) Sato et al. (2007)	Basharat et al. (2016)	0.58 (0.56)	0.029 (0.030)	8.2	30	26	27	0.94	0.93	0.93			
	(K_{BS}) Basharat et al. (2016)	Sato et al. (2007)	0.09 (0.09)	0.002 (0.002)		0.2	-7	-5	0.72	0.69	0.69			
Aisen (A)														
	(A_{GS}) Gorum et al. (2014)	Sepulveda et al. (2010)	0.52 (0.52)	0.010 (0.009)	29.7	56	39	39	0.93	0.93	0.93			
	(A_{SG}) Sepulveda et al. (2010)	Gorum et al. (2014)	0.4 (0.41)	0.006 (0.006)		6	5	5	0.77	0.78	0.78			
Wenchuan (W)														
	(W_{LX}) Li et al. (2014)	Xu et al. (2014)	0.35 (0.35)	0.026 (0.029)	14.0	36	26	27	0.87	0.85	0.85			
	(W_{XL}) Xu et al. (2014)	Li et al. (2014)	0.19 (0.19)	0.011 (0.012)		62	50	51	0.86	0.84	0.84			
Haiti (H)														
	(H_{HG}) Harp et al. (2016)	Gorum et al. (2013)	0.24 (0.21)	0.001 (0.001)	18.8	-51	-74	-73	0.88	0.84	0.84			
	(H_{GH}) Gorum et al. (2013)	Harp et al. (2016)	0.64 (0.62)	0.005 (0.007)		-52	-62	-60	0.9	0.83	0.83			
Gorkha (G)														
	(G_{WR}) Watt (2016)	Roback et al. (2018)	0.27 (0.33)	0.004 (0.005)	22.8	22	1	1	0.92	0.92	0.92			
	(G_{RW}) Roback et al. (2018)	Watt (2016)	0.42 (0.43)	0.008 (0.008)		20	7	6	0.94	0.93	0.93			
	(G_{RZ}) Roback et al. (2018)	Zhang et al. (2016)	0.1 (0.09)	0.001 (0.001)	8.3	30	-4	-3	0.92	0.90	0.90			
	(G_{ZR}) Zhang et al. (2016)	Roback et al. (2018)	0.49 (0.51)	0.004 (0.005)		19	4	5	0.96	0.95	0.95			
	(G_{ZW}) Zhang et al. (2016)	Watt (2016)	0.11 (0.11)	.0003 (.0003)	11.1	-28	-47	-47	0.92	0.92	0.92			
	(G_{WZ}) Watt (2016)	Zhang et al. (2016)	0.79 (0.80)	0.010 (0.010)		-9	-17	-17	0.97	0.97	0.97			
		Median	0.38	0.006	14.0	20	3	3	0.92	0.91	0.91			
		Mean	0.37	0.008	16.1	10	-4	-3	0.89	0.88	0.88			

1005